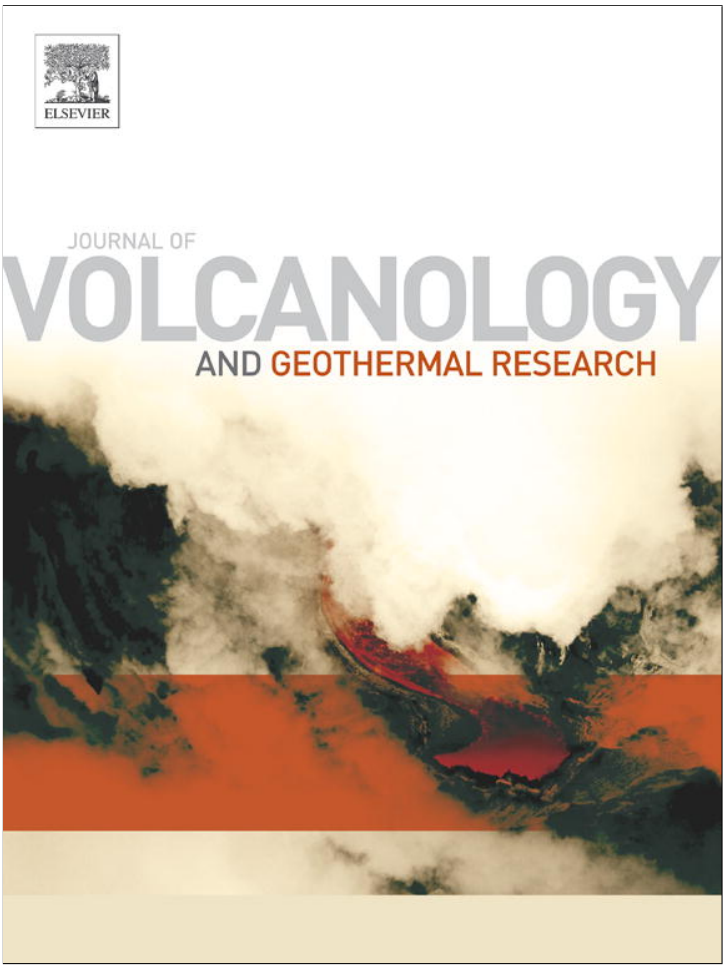

Journal of Volcanology and Geothermal Research 260 (2013) 103–116

Contents lists available at SciVerse ScienceDirect

Journal of Volcanology and Geothermal Research

journal homepage: www.elsevier.com/locate/jvolgeores

Timing and composition of volcanic activity at Harrat Lunayyir, western Saudi Arabia

Robert A. Duncan [a,b,*], Abdullah M. Al-Amri [a]

[a] Department of Geology & Geophysics and DSFP, King Saud University, Riyadh, Saudi Arabia
[b] College of Earth, Ocean, and Atmospheric Sciences, Oregon State University, Corvallis, USA

ARTICLE INFO

Article history:
Received 14 January 2013
Accepted 14 May 2013
Available online 26 May 2013

Keywords:
Continental volcanism
$^{40}Ar/^{39}Ar$ age determinations
Trace elements
Mantle melting

ABSTRACT

Harrat Lunayyir is an alkali basaltic, continental volcanic field in NW Saudi Arabia. Lava flows and cinder cones are basanite to alkali olivine basalt to trachy-basalt in composition. The field contains about 50 volcanic cones fed by fissures through Precambrian crystalline rocks along a N–S axis, lying about 200 km east of the Red Sea spreading center. One of cones erupted as recently as the 10th century AD. Analysis of a recent earthquake swarm (2007–2009) indicates a ~10-km, NW-trending cluster of events at both shallow and deep crustal locations, concentrated in regions of higher velocity material. Six volcano-stratigraphic units are identified, based on super-position and morphology (degree of erosion). New ^{40}Ar–^{39}Ar incremental heating age determinations indicate that the entire volcanic history occurred within the last 600 ka, with eruption rate decreasing with time. Major and minor element compositional variations are due almost entirely to crustal level fractionation (of mainly olivine, plagioclase, and clinopyroxene), or small differences in mantle partial melting. Primitive liquid composition, estimated by adding olivine to parental magma compositions, is consistent with ~10% melting of an upper mantle peridotitic source in the depth range of spinel to garnet stability (80–60 km). There is no evidence for crustal assimilation. Trace element variations (in Dy/Yb, Ce/Yb) are consistent with shallowing of the asthenospheric melting region with time. Regional variations in trace element compositions among other harrats indicate a strong influence of the lithosphere–asthenosphere boundary in controlling mantle melting.

1. Introduction

Extensive Cenozoic basaltic lava fields occur in the western part of the Arabian peninsula (Fig. 1), forming one of the largest alkali basalt provinces in the world (area: 180,000 km^2). These young volcanic fields (called "harrats") lie within 300 km of the NW-trending eastern margin of the Red Sea. There is no counterpart to these volcanic centers on the western margin (African Plate) of the Red Sea. Likewise, topography is more elevated and rugged on the Arabian side, compared with the African side (Bohannon et al., 1989). In contrast to the tholeiitic basalts of the Red Sea spreading system, lava compositions in this province include tholeiites but are predominantly basanite to alkali olivine–basalt to hawaiite, with minor more evolved compositions. Within several large centers, volcanic activity began (>12 Ma) with tholeiitic to transitional compositions, then became more alkalic for younger eruptions (<12 Ma) (Camp and Roobol, 1992). The older period of activity includes dikes and eruptive centers close to and aligned with the NW–SE Red Sea margin, while the younger volcanic centers are distributed over a 200 km swath and display N–S alignment. The most voluminous centers form a prominent N–S volcanic axis, the Makkah–Madinah–Nafud (MMN) line. This lineament is aligned with the Ha'il–Rutbah Arch axis of uplift of the Arabian shield, a Late Cretaceous–Early Tertiary structure that was reactivated ~15 Ma (Coleman, 1993).

Harrat Lunayyir is one of the smaller and younger volcanic fields, lying ~100 km east of the Red Sea margin and on the western edge of the escarpment. It is located NW of Al-Madinah Al Munawwarah, north of Yanbu and in the immediate vicinity of the town of Al Ays between latitudes 24°50'N to 25°29'N and longitudes 37°28'E to 38°04'E., occupying a surface area of about 3575 km^2 (Fig. 2). This study was initiated because Harrat Lunayyir experienced multiple seismic swarms in the period 2007–2009. Recent studies (e.g. Pallister et al., 2010) have indicated that these swarms are associated with magma that has risen to shallow levels beneath Harrat Lunayyir, potentially increasing the likelihood of a volcanic eruption. It is estimated that at least twenty-one different eruptions have occurred in western Arabia over the past 1500 yr (Camp et al., 1987), including one within Harrat Lunayyir about 1000 yr ago. The Harrat Lunayyir area is characterized by geothermally warm groundwater where temperatures up to 32 °C were measured in April 2007 before the earthquake swarm began. Farmers in the Harrat Lunayyir area reported seeing steam in many places on cold winter mornings, while geothermal anomalies and

* Corresponding author at: College of Earth, Ocean and Atmospheric Sciences, 104 CEOAS Admin Building, Oregon State University, Corvallis, OR 97331, USA. Tel.: +1 541 737 5213.
E-mail addresses: rduncan@coas.oregonstate.edu (R.A. Duncan), seismology333@gmail.com (A.M. Al-Amri).

0377-0273/$ – see front matter © 2013 Elsevier B.V. All rights reserved.
http://dx.doi.org/10.1016/j.jvolgeores.2013.05.006

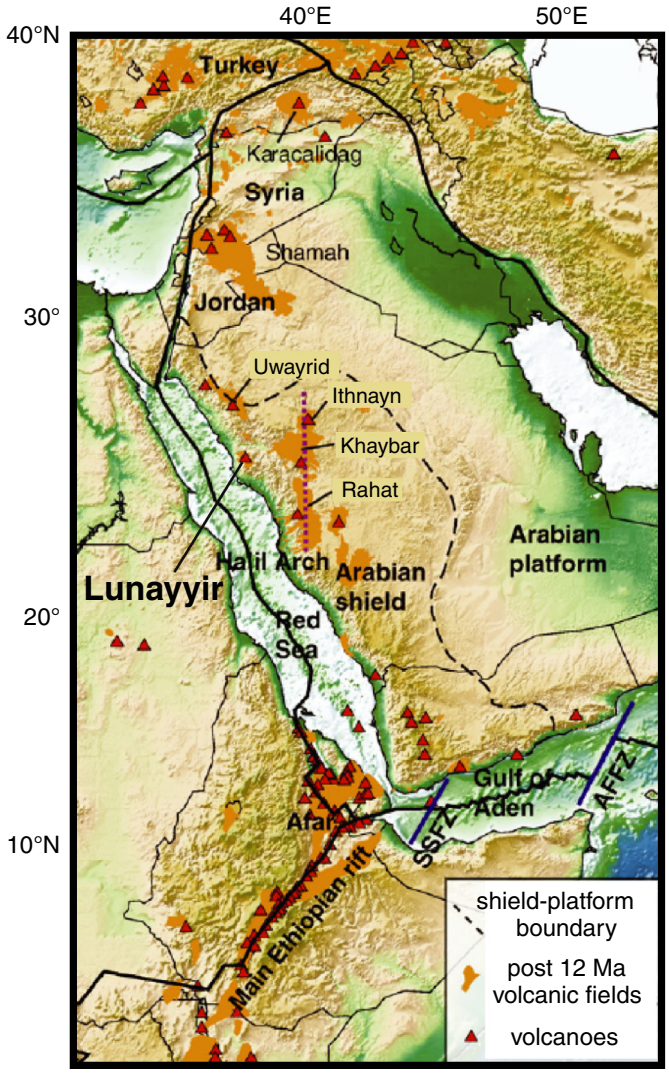

Fig. 1. Location map for volcanic fields ('harrats') in western Saudi Arabia (from Chang and van der Lee, 2011). Individual harrats lie within 300 km of the Red Sea margin, but eruptive centers/fissures are aligned predominantly N–S. The most voluminous provinces fall within the region indicated by dotted red line (Ha'il Arch), also called the Makkah–Medinah–Nafud (MMN) lineament. Harrat Lunayyir is a relatively small province that lies between the MMN line and the Red Sea. (For interpretation of the references to color in this figure legend, the reader is referred to the web version of this article.)

reports of stream were first noted by Saudi Geological Survey staff in 2001. The current phase of Harrat Lunayyir activity is therefore considered to have begun at least 10 yr ago.

Various ideas have been proposed for the origin of the aligned volcanic fields of western Saudi Arabia. The timing and proximity to the Red Sea spreading system have led some researchers to favor plate extension and lithospheric thinning, increasing from east to west (Bertrand et al., 2003; Shaw et al., 2003). The triple junction to the south, formed by Red Sea, Gulf of Aden and East African Rift plate separation, has been proposed to have initiated at the onset of Afar hotspot activity (~32 Ma) (Schilling, 1973; Courtillot et al., 1984; Hill et al., 1992; Baker et al., 1995, 1997; Debayle et al., 2001). Radial flow of upper mantle material from the underlying mantle plume may have reached the base of the lithosphere beneath the Arabian shield, leading to excess heat, thinning, uplift and melting (Camp and Roobol, 1992; Krienitz et al., 2009). A separate mantle plume, upwelling beneath the Arabian shield, has been implicated from the distribution of the volcanic activity (Moufti and Hashad, 2005) and seismic imaging (Chang and van der Lee, 2011).

The main objective of this paper is to report new age determinations that define the timing and duration for the Harrat Lunayyir volcanic activity, and describe the petrology and geochemical characteristics of the lavas. We then compare Harrat Lunayyir compositions with neighboring fields and discuss possible models for dynamic controls on the timing and composition of the regional volcanic activity.

2. Geologic mapping and volcanic stratigraphy

The Cenozoic to recent basaltic lava fields of western Saudi Arabia rest directly on rocks of the stable Precambrian Arabian shield (Fig. 1). These older rocks are upper Proterozoic metavolcanics and plutons of mainly granitic composition. They rise as rugged hills around and within the lava field. Harrat Lunayyir is constructed from a series of volcanic eruptions that took place along related fissures, producing ~50 cinder cones that form N–S and NW–SE trends and cover an area of about 3600 km^2. Flow morphology is predominantly a'a type, and thicknesses are typically 3–5 m. Scoria cones are typically 400–500 m in diameter and 100–200 m in height.

A geological map has been prepared (Fig. 2, after Al-Amri et al., 2012), and determined from field investigation, geomorphologic data, satellite imaging and petrographic examination. Precambrian rocks of Pan-African mobile belt age occupy the northern and the southern parts, and also the eastern periphery of the mapped area. In the central zone the Precambrian rocks form isolated inliers. During volcanic eruptions the relief of the Precambrian rock was apparently great enough to hinder the lavas flowing westwards. Field observations lead to the identification of the following volcanic units (young to old), based primarily on degree of erosion, saturation with wind-blown dust, and relative stratigraphic position (Al-Amri et al., 2012), based on the characteristics used by Camp et al. (1989):

Q5 — Historic to late Prehistoric lava flows.
Q4 — Prehistoric lava flows and scoria cones.
Q3 — Non-eroded lava flows and scoria cones.
Q2 — Eroded lava flows and scoria cones.
Q1 — Eroded lava flows without scoria cones.
Unconformity (thin, intermittent soil horizon).
T "Tertiary" basalt.

There are no systematic changes in the composition of the lava flows among the volcanic units.

Based on the Al-Amri et al. (2012) map, we have estimated erupted volumes for each of the volcanic units from areal extent and observed thicknesses, assuming that older units continue beneath younger units. These are: Q5 (7.2 km^3), Q4 (11.5 km^3), Q3 (16.1 km^3), Q2 (4.3 km^3), Q1 (13.7 km^3), and T (18.0 km^3). When divided by the estimated duration of each unit's activity (Age determinations by ^{40}Ar/^{39}Ar incremental heating section below) we derive eruption rate estimates.

3. Seismicity and earthquake locations

Recently, Hansen et al. (in press) observed two linear NW-trending clusters of ~1300 seismic events (Fig. 3). The northern cluster is approximately 5 km long and the southern cluster is about 3 km long. At the south end of the swarm there is a dense cluster of earthquake locations beneath a volcanic center. The earliest events are intermediate depth (5–9 km) along the northern linear swarm, as well as deep events (>9 km) beneath the southern volcanic center. As the swarm continued up to July 2009, the second linear swarm developed. This cluster of earthquakes defines a steeply dipping plane that connects the deeper region of seismicity with that closer to the surface. Most of the seismicity, across the entire depth range, is concentrated in regions of higher velocity material. The planar dipping

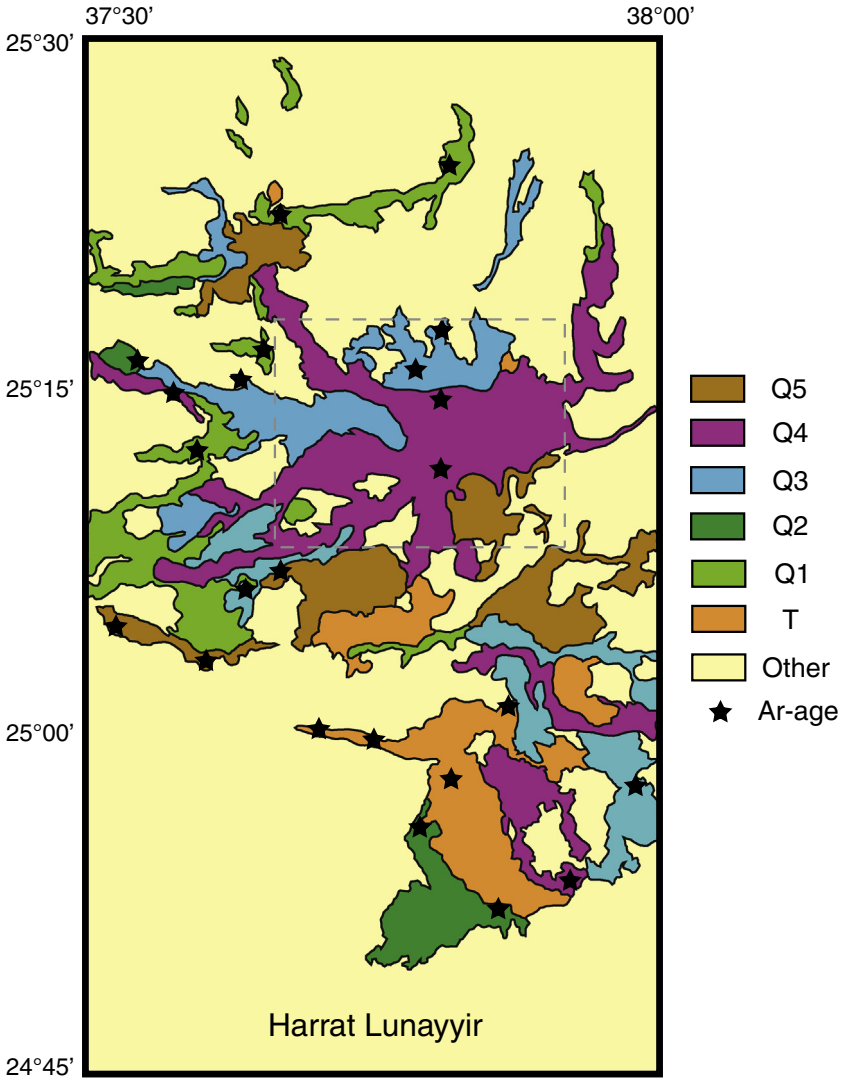

Fig. 2. Simplified geologic map of the Harrat Lunayyir area, showing the distribution of volcanic units mapped as Tertiary (T) and Quaternary (Q1 to Q5 in decreasing age). "Other" includes Pan-African age shield rocks and alluvium (after Al-Amri et al., 2012). Black stars are locations of dated samples; gray dashed line shows location of Fig. 3.

cluster occurs over a region of slower velocity to the north, and slow velocity material also bounds the shallow seismicity cluster (Hansen et al., in press).

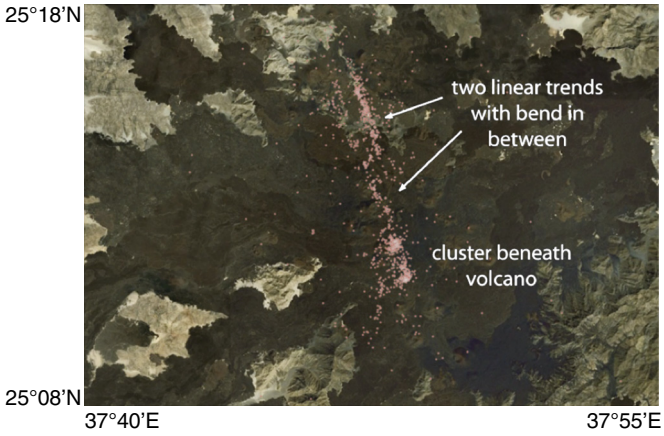

Fig. 3. Seismic event relocations (pink dots) for Harrat Lunayyir 2009 earthquake swarm. Two linear NNW-trending clusters are seen, covering a distance of approximately 10 km, as well as a more pronounced cluster beneath a volcanic center at the south end of the distribution.

Pallister et al. (2010) investigated the same seismic swarm with InSAR methods, and concluded that the surface deformation is best modeled by intrusion of a NNW-trending, ~10-km dike to shallow depth (1–2 km). These authors speculated that deformation in the Harrat Lunayyir area may indicate that extension of continental lithosphere well to the east of the Red Sea rifted margin may be ongoing. Hansen et al. (in press) note the coincidence of inferred dike location and orientation with the 2007–2009 Harrat Lunayyir seismic swarm, and speculate that the seismicity was associated with volcanic expansion of the dike in the subsurface. They further interpret the region of fast velocities (relative to surrounding crust) as a zone of repeated magmatic intrusion.

4. Petrography

We prepared representative thin sections and examined them petrographically. The samples are invariably vesicular and occasionally porphyritic (generally <5% phenocrysts). Vesicles are rarely filled with secondary calcite and zeolites and display a typical amygdaloidal texture. The phenocrysts are dominantly forsteritic olivine (Fo_{90-70}), which quite often has a skeletal form or corrosion embayments thus indicating some disequilibrium with the melt. Plagioclase phenocrysts are also present in some rocks, being dominantly labradorite (An_{70-60}).

The clinopyroxene is dominantly titanaugite with a pronounced light brown color in plane polarized light. It forms ophitic and subophitic textures with plagioclase. Opaques are present either in euhedral grains or in the form of anhedral granules dispersed in the groundmass composed of plagioclase laths, clinopyroxenes and rarely olivine with some apatite and other accessory minerals. In most of the porphyritic samples olivine is the main phenocryst phase; clinopyroxene is very rare; plagioclase is present as phenocrysts in a few of the more primitive compositions and as groundmass laths in the more evolved compositions. We did not observe any xenoliths in these samples, although both crustal and mantle xenoliths are reported from other harrat volcanic fields (e.g., Coleman, 1993).

5. Age determinations by $^{40}Ar/^{39}Ar$ incremental heating

Previous attempts to determine the ages of Harrat Lunayyir rocks have been based on the K–Ar total fusion method (summarized in Camp and Roobol, 1992) and are predominantly Quaternary age (one sample reported at ~7 Ma). On this basis, Al-Amri et al. (2012) proposed that volcanic activity began as early as late Miocene–Pliocene time. However, 6 lavas were dated by them using the $^{40}Ar/^{39}Ar$ incremental heating method, one each from the 6 volcanic units, and all gave ages less than 1 Ma (Table 1). The $^{40}Ar/^{39}Ar$ incremental heating method offers advantages over the K–Ar method, historically used for age determinations in volcanic provinces. While alteration of primary phases to secondary clays is not a major problem in this very arid region, the known contribution of mantle-derived Ar from phenocryst phases (especially olivine) and the occurrence of mantle xenoliths in harrat lavas (Coleman, 1993) could produce erroneously old measured ages. For these reasons, we chose to analyze phenocryst- and xenolith-free groundmass separates. Incremental heating experiments allow examination of the step-wise release of Ar with increasing temperature for evidence of mantle-derived ("excess") ^{40}Ar.

Some 18 new samples were dated using the $^{40}Ar/^{39}Ar$ incremental heating technique from the 6 volcano–stratigraphic units mapped in the Harrat Lunayyir volcanic field. We collected samples from the different flow units following the geological map of Al-Amri et al. (2012). The samples are compact, fine-grained basanites, alkali olivine basalts and trachy–basalts, showing aphyric to only moderately phyric textures. In these rocks, the phenocrysts are mainly olivine and plagioclase, and the groundmass consists mainly of glass and micro- to cryptocrystalline plagioclase, and augite with minor olivine.

We followed sample procedures described by Duncan and Keller (2004). Briefly, fresh samples were reduced in a small jaw crusher with alumina surfaces, followed by sieving to obtain the 300–600 μm size fraction. We then separated the groundmass fraction from phenocrysts by hand-picking under binocular microscope. The separates were further cleaned by mild acid-leaching (1 N HNO_3 for ~20 min) in an ultrasonic bath that was heated to approximately 50 °C. Finally, the leached separates were washed in ultraclean water and dried in an oven (~70 °C). Samples were wrapped in Cu foil, loaded in evacuated quartz tubes, alternating with packages of FCT-3 biotite monitor standard (28.04 Ma; Renne et al., 1998), and irradiated for 6 h in the Oregon State University TRIGA reactor ICIT facility. Values of the irradiation parameter *J* for individual sample positions were calculated by parabolic interpolation between the measured monitors. Estimated uncertainties for *J* are between 0.2% and 0.3%. Corrections for interfering reactions involving Ca and K are given in Wijbrans et al. (1995).

The incremental heating $^{40}Ar/^{39}Ar$ age determinations were performed on crystalline 300–600 μm groundmass separates using a continuous, 10 W CO_2 laser probe connected to a MAP-215/50 mass spectrometer at Oregon State University. The mass spectrometer is a 90° sector instrument with a Nier-type source and an all-metal extraction system for gas cleanup prior to Ar-isotopic measurements. The mass spectrometer has an electron multiplier for high sensitivity and an electrostatic analyzer with adjustable collector slit for an effective resolution (~600) of Ar peaks from any small hydrocarbon peaks. We loaded up to 80 mg of irradiated groundmass samples into Cu-planchettes, which are then pumped within a sample chamber fitted with a ZnS window transparent to the CO_2 laser wavelength. Software allows for scanning across samples in a preset pattern with a defocused beam, to evenly heat the material. Gas cleanup

Table 1
^{40}Ar–^{39}Ar age determinations for lavas from Harrat Lunayyir, NW Saudi Arabia.

Sample	Formation	Integrated Age (Ma)	1σ error (ka)	Plateau age (ka)	1σ error (ka)	N	MSWD	Isochron age (ka)	1σ error (ka)	$^{40}Ar/^{36}Ar$ initial	1σ error
HL-1	Q5	109	116	**45**	**78**	6/7	0.67	−23	204	306	80
HL-2	Q5	−50	118	Not reported		8/9	0.58	**5**	**81**	296	*
HL-40	Q5	137	87	**78**	**71**	7/7	0.63	30	166	303	73
HL-26	Q4	352	111	Not reported		7/8	0.76	**191**	**82**	296	*
HL-15	Q4	257	102	**285**	**83**	7/7	0.59	161	241	302	28
HL-38	Q4	525	70	**189**	**47**	6/8	0.56	58	116	303	11
HL-39	Q4	223	96	**208**	**85**	7/7	0.15	180	250	297	36
HL-35	Q3	95	109	Not reported		12/12	0.36	**149**	**110**	296	*
HL-20	Q3	166	57	**131**	**45**	8/8	0.25	117	89	296	12
HL-29	Q3	392	79	**356**	**69**	8/8	1.03	356	92	292	22
HL-36	Q3	372	71	**351**	**47**	7/7	0.89	288	75	302	36
HL-9	Q2	517	66	**302**	**37**	7/8	0.84	238	84	300	12
HL-14	Q2	478	113	Not reported		7/10	0.46	**511**	**78**	296	*
HL-19	Q2	390	79	**312**	**47**	7/7	1.11	250	63	300	24
HL-27	Q2	*1830*	*145*	*1210*	*130*	*6/8*	*0.40*	*1190*	*185*	*297*	*21*
HL-25	Q1	787	62	**437**	**48**	5/8	0.81	348	82	302	10
HL-31	Q1	277	121	Not reported		9/11	0.44	**256**	**83**	296	*
HL-32	Q1	192	93	**48**	**59**	6/7	1.06	36	65	296	4
HL-33a	Q1	560	67	**406**	**51**	6/7	0.85	340	66	343	127
HL-33b	Q1	517	65	**436**	**50**	7/7	1.00	355	63	300	4
HL-3	T	579	96	**434**	**91**	6/7	1.42	378	120	298	7
HL-5	T	490	89	**474**	**60**	8/8	0.60	464	67	297	12
HL-8	T	642	106	**569**	**77**	7/7	0.67	503	86	297	2
HL-17	T	172	304	Not reported		12/12	0.36	**325**	**89**	296	*

Ages calculated using biotite monitor FCT-3 (28.04 Ma) and the total decay constant λ = 5.530E-10/yr. N is the number of heating steps (defining plateau/total).
MSWD is an F-statistic that compares the variance within step ages with the variance about the plateau age. J combines the neutron fluence with the monitor age.
Preferred ages are shown in bold; italics indicate sample with suspected mantle-derived (excess) ^{40}Ar.
* Sample ages reported by Al-Amri et al. (2012); isochron age fixed to atmospheric intercept.

was accomplished with a series of Zr–Al getters. All argon ages were calculated using the corrected Steiger and Jäger (1977) decay constant of 5.530 ± 0.097 × 10^{-10} yr^{-1} (2σ) as reported by Min et al. (2000).

Incremental heating plateau ages were calculated as weighted means (by inverse variance) and isochron ages as YORK2 least-square fits with correlated errors (York, 1969) using the ArArCALC v2.2 software from Koppers (2002) that is available from the http://earthref.org/tools/ararcalc.htm website. In this paper, all errors on the $^{40}Ar/^{39}Ar$ ages are reported at the 1σ level. In general, samples produced plateaus in age spectrum plots, composed of 6–12 step heating ages representing 77–100% of the total ^{39}Ar released (Fig. 4a). In such cases, corresponding isochron ages are consistent with the plateau ages. We interpret these as reliable crystallization ages. Table 1 summarizes the results of our new geochronological data and previous $^{40}Ar/^{39}Ar$ incremental heating experiments; full data tables and figures are available for 18 new age determinations at the EarthRef database (http://earthref.org/). The 6 ages reported by Al-Amri et al. (2012) are isochron ages, constrained to pass through the composition of atmospheric Ar ($^{40}Ar/^{36}Ar$ = 295.5); the assumption being that these magmas were fully outgassed and equilibrated with the atmosphere on eruption.

One of our samples, HL-27, provided a plateau age of 1.21 ± 0.13 Ma, based on 6 of 8 step ages, that is significantly older than any of the other samples (Fig. 4b). It was collected from mapped volcanic unit Q2, above older units Q1 and T that show an age range of 300–600 ka. The two lowest temperature steps, not used in the plateau age calculation, provided older ages that appear to have an excess ^{40}Ar component. Using all steps in an isochron calculation yielded an age of 970 ± 290 ka, with an initial $^{40}Ar/^{36}Ar$ composition of 312 ± 4. Hence, there is evidence from the disturbed age spectrum, the isochron analysis, and most significantly from the stratigraphic position that this sample has some small amount of excess ^{40}Ar, probably in xenocrystic olivine not completely removed, and its measured age is not considered reliable. Another sample, HL-32, gave a very young plateau age (48 ± 59 ka) relative to its stratigraphic position (unit Q1). In this case, the age spectrum looks undisturbed and we see no reason to discount the measured age. We are left with speculating that the sample actually came from a younger unit (i.e., incorrectly mapped or located).

We plot the 23 reliable $^{40}Ar/^{39}Ar$ ages in a histogram, along with a probability density distribution (Fig. 5) that shows more or less continuous volcanic activity from about 600 ka to the present, with perhaps some peaks of activity at ~400 ka and ~200 ka. We see no period of inactivity that could provide a significant unconformity. If we now assign age ranges to the volcano-stratigraphic units identified in mapping, we can estimate eruption rates through time by dividing our volume estimates by the durations. These are displayed in Fig. 6, showing that eruption rates have decreased (except for period Q2) by an order of magnitude from initial activity to the present.

6. Geochemical analyses

We had 43 rock samples analyzed by ALS Environmental Laboratories (Canada) for major, trace and rare earth element concentrations. Fresh chips of each sample were crushed and split to obtain a representative portion, then pulverized in a tungsten carbide swing mill. The whole rock powders were then used to determine major and minor element oxide concentrations (reported as weight %, Table 2) using X-ray fluorescence spectroscopy. An ignited sample (0.9 g) is added to 9.0 g of lithium borate flux (50%–50% $Li_2B_4O_7$–$LiBO_2$), mixed well and fused in an auto fluxer between 1050 and 1100 °C. A flat molten glass disc is prepared from the resulting melt for X-ray analysis. Totals of major and minor oxides (Table 2) are typically 98–100%, confirming the generally unaltered appearance of these rocks. Trace and rare earth element concentrations were determined using ICP-AES and ICP-MS methods. A

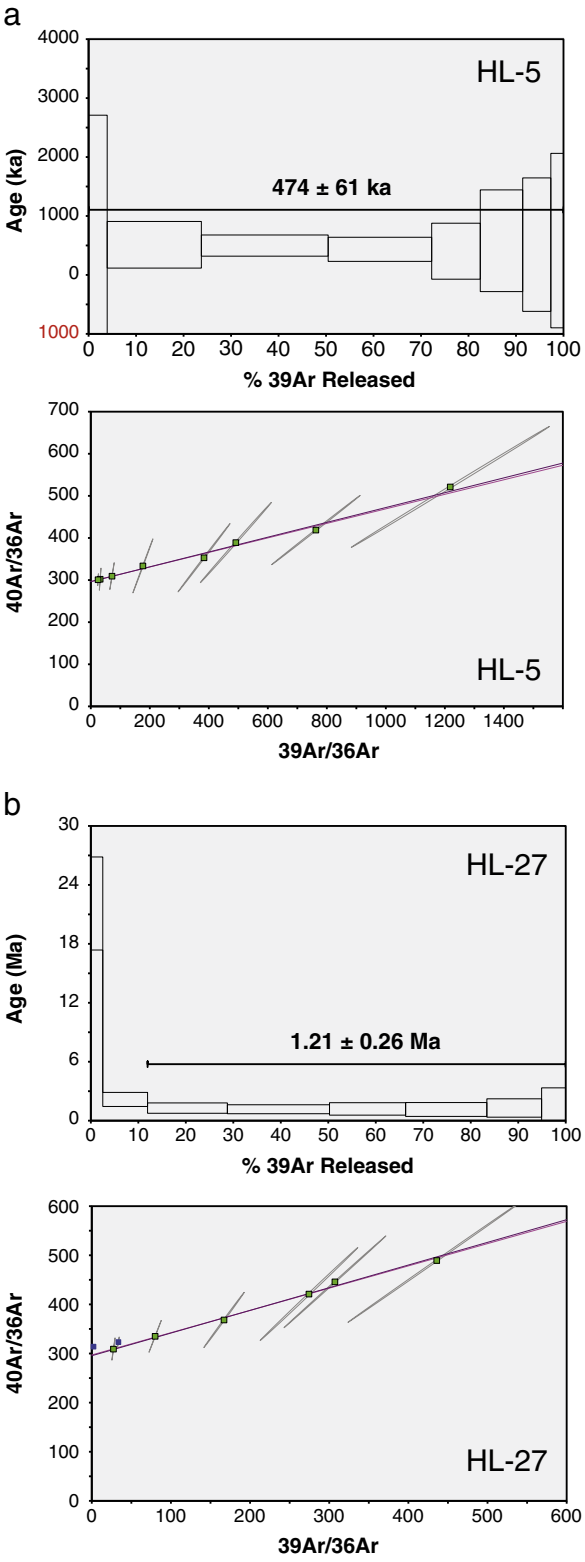

Fig. 4. Representative age spectra (plateaus) and isochron plots derived from $^{40}Ar/^{39}Ar$ incremental heating experiments on Harrat Lunayyir basaltic lavas. Plateau age (±1σ) is calculated from the weighted mean of individual step ages whose width is the proportion of total sample ^{39}Ar released and whose height is 2σ error. (a) sample HL-5, in which all steps are used in the plateau and isochron age calculations; (b) sample HL-27, in which excess ^{40}Ar is observed in at least the first 2 steps (not used in calculations). Including all steps in the isochron calculation produces a younger age and non-atmospheric initial $^{40}Ar/^{36}Ar$.

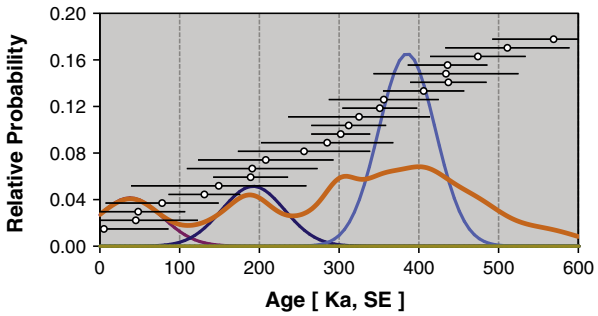

Fig. 5. Histogram of measured 17 new plateau ages and 6 isochron ages (Al-Amri et al., 2012) for lavas from Harrat Lunayyir. The orange curve is a probability density curve (ideogram) for all data, which can be decomposed into three possible intervals of peak volcanic activity. The simplest interpretation, however, is that eruptions occurred rather continuously from about 600 ka to the present.

prepared powdered sample (0.200 g) is added to lithium metaborate/lithium tetraborate flux (0.90 g), mixed well and fused in a furnace at 1000 °C. The resulting melt is then cooled and dissolved in 100 mL of 4% nitric acid/2% hydrochloric acid. This solution is then analyzed by ICP-AES and ICP-MS instruments and the results are corrected for spectral inter-element interferences. Concentrations of trace and rare earth elements are reported in parts per million (ppm) and detection limits are sub-ppm.

The Harrat Lunayyir volcanic suite displays narrow major element ranges, that vary from 43.8 to 47.2 wt.% SiO_2, 15.4–17.0 wt.% Al_2O_3, 9.8–15.9 wt.% Fe_2O_3, 7.1–12.8 wt.% CaO, 4.3–8.7 wt.% MgO, 2.72–4.57 wt.% Na_2O, 0.36–1.43 wt.% K_2O, 1.63–3.2 wt.% TiO_2, 0.16–0.25 wt.% MnO, and 0.22–0.87 wt.% P_2O_5. The Mg# = (molar MgO / MgO + FeO) * 100, assuming a Fe^{+}_{2}/Fe total ratio of 0.85, ranges between 35 and 59. These values indicate that none of the samples represents a primary magma. The samples plot exclusively in the basanite, alkali olivine basalt, and trachy-basalt fields on the total alkalis vs silica diagram (Fig. 7). All samples plot in the field of alkali basalts rather than tholeiitic basalts.

The similarity of the basalts of different episodes indicates that the parent magma changed very little in composition throughout the volcanic history. Major and trace elements are plotted versus Mg# as an index for differentiation (Figs. 8 and 9). Na_2O, K_2O, Fe_2O_3, TiO_2, and

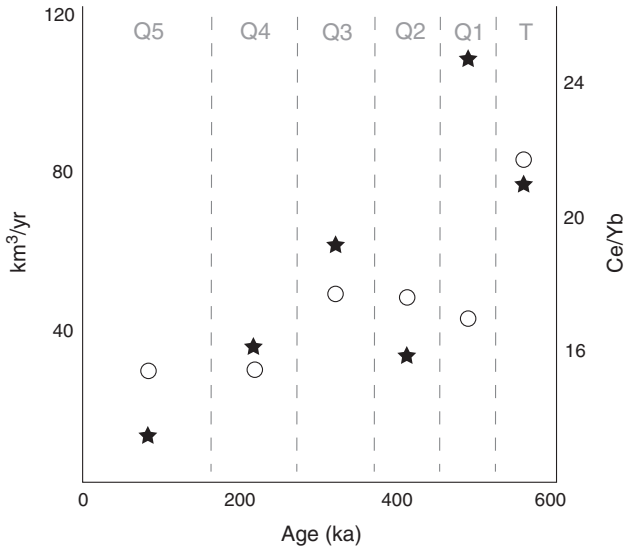

Fig. 6. Eruption rates (black stars) through time during construction of Harrat Lunayyir. Estimated volumes divided by age ranges of 6 mapped volcano–stratigraphic units (T, Q1 to Q5) show an order of magnitude decrease from initial activity up to the present. The trace element ratio Ce/Yb (open circles) tracks the depth of melt separation from the mantle (Ellam, 1992), and appears to indicate a thinning lithospheric "lid".

P_2O_5 increase with decreasing Mg#, while CaO decreases with differentiation reflecting the separation of both clinopyroxene and plagioclase. SiO_2 displays no systematic variation with differentiation. On the other hand, Al_2O_3 increases at early stages during olivine and pyroxene fractionation and decreases when plagioclase becomes a significant fractionating phase. Thus, it appears that low pressure fractional crystallization can account for the observed variation in the rocks of the successive basalt flows. Compositional variation within each volcano–stratigraphic unit ranges from relatively primitive to only moderately evolved, indicating that crustal residence time did not change significantly with time. This contrasts with evidence at the longer-lived centers Harrats Khaybar, Ithnayn and Kura (Fig. 1), where compositionally distinct parental magmas (olivine transitional basalt to alkali olivine basalt to hawaiite in decreasing age) were produced through the volcanic history (Camp et al., 1991). Crystallization modeling using the pMELTS software (Ghiorso et al., 2002) for two of the more primitive lava compositions yields liquidus temperatures around 1200 °C. Addition of olivine only to the most primitive rock compositions (e.g., HL-8) produces a likely parental melt composition (Mg# ~ 70). Comparison of this composition with the products of experimental studies of melting of a range of upper mantle peridotite compositions (Falloon et al., 1988) suggests that such magmas could have been formed by ~10% melting at 20–25 kbar (75–60 km depth).

The Harrat Lunayyir basalts further exhibit a compositional range in trace elements, with generally smooth concentration variations with Mg#. Selected trace elements are plotted versus Mg# (Fig. 9). Ni and Cr show decreasing concentrations with decreasing Mg# demonstrating compatibility in olivine fractionation; Rb, Y, Zr, Nb, and Ba are incompatible elements and increase with decreasing Mg#. Strontium, on the other hand, mimics the trend of Al_2O_3, with an increasing trend at early stages during the fractionation of ferromagnesian minerals and a decreasing trend at the onset of plagioclase fractionation. The subset of unit T samples with higher Sr is also often plagioclase-phyric. Most incompatible elements, including the high field strength elements (HSFE), show a negative correlation with Mg#. Trace element binary plots (e.g., P_2O_5 vs Zr, not shown) exhibit linear correlations and confirm the open system fractionation control on compositional variation. Ratios of similarly incompatible trace elements, e.g., Th/Ta, do not change with trace element concentration (Th ppm), indicating a uniform mantle source for partial melting. Trace element discrimination plots (e.g., Zr/Y vs Ti/Y or Nb/Y vs Zr/Y) place Harrat Lunayyir compositions firmly in "within plate" tectonic settings rather than a plate margin (MORB) association (e.g., Irvine and Baragar, 1971). In spite of forming from magmas that have traversed thick continental lithosphere, and which transported a range of crustal and upper mantle xenoliths observed at other harrat fields (Coleman, 1993), the Harrat Lunayyir lavas show no evidence of significant crustal assimilation in either major, minor and trace element variations, or in isotopic compositions (Altherr et al., 1990) which fall in a narrow, unradiogenic range ($^{87}Sr/^{86}Sr$: 0.7029–0.7031; $^{143}Nd/^{144}Nd$: 0.51290–0.51293).

The Harrat Lunayyir lavas exhibit uniformly light rare earth element (LREE) enriched patterns (chondrite-normalized, Fig. 10), whose variability can be explained in large part by fractional crystallization. Again, we see no significant differences in range of concentrations among the volcano–stratigraphic units (panels in Fig. 10). The parameter La/Yb measures the steepness of the rare earth patterns, and ranges from 14.5 to 5.2 (Table 2). In detail, however, we see that average La/Yb for the volcano-stratigraphic units decreases smoothly from 10.8 for unit T (oldest) to 6.8 for Q5 (youngest). There is no correlation with Mg#, as would be expected from low-pressure fractional crystallization within units. There is a distinct flattening of the heavy REE slopes compared with the overall patterns: Dy/Yb ranges from 2.07 to 1.87 (Table 2), again decreasing from oldest to youngest units. Because the heavy rare earths show a

Table 2
Geochemical data for lava flows, Harrat Lunayyir, NW Saudi Arabia.

Formation	Tertiary	Tertiary	Tertiary	Tertiary	Tertiary	Tertiary	Tertiary	Tertiary	Tertiary	Tertiary	Tertiary	Tertiary	Q1	Q1	Q1	Q1
Sample	HL 3	HL 4	HL 5	HL 6	HL 7	HL8	HL1O	HL11	HL13	HL17	HL18	Average	HL 20	HL 21	HL 25	HL 31
Latitude (N)	24° 59.55′	24° 59.20′	24° 59.01′	24° 58.60′	24° 57.87′	24° 56.88′	24° 58.43′	24° 57.87′	24° 53.98′	24° 58.25′	24° 58.31′		25° 06.25′	25° 06.78′	25° 11.68′	25° 22.61′
Longitude (E)	37° 43.28′	37° 44.84′	37° 45.90′	37° 47.71′	37° 48.60′	37° 48.85′	37° 49.52′	37° 50.27′	37° 52.10′	37° 54.05′	37° 55.91′		37° 39.40′	37° 39.77′	37° 36.55′	37° 40.48′
SiO_2	45.67	46.17	46.32	46.12	47.1	44.91	46.85	46.31	46.21	45.39	45.44	46.04	45.43	43.98	45.32	46.77
Al_2O_3	15.75	16.01	16.44	16.35	16.61	15.37	16.74	16.65	16.62	16.21	16.51	16.30	15.94	15.62	15.75	16.63
Fe_2O_3	11.7	12.62	11.79	12.18	13.43	11.85	12.49	13.11	11.32	13.99	12.63	12.46	15.1	12.34	12.03	15.41
CaO	9.82	9.18	9.25	9.01	7.74	10.37	8.94	9	8.85	9.13	9.87	9.20	7.63	11.21	9.65	7.05
MgO	7.33	7.45	6.78	6.47	4.6	7.97	6.66	6.68	5.78	6.27	7.04	6.64	4.68	7.58	7.02	4.59
Na_2O	3.79	3.86	3.57	3.61	4.51	3.15	4.15	3.84	3.67	3.55	3.33	3.73	4.18	2.86	3.69	4.57
K_2O	1.02	0.81	0.85	0.84	1.37	0.99	0.86	0.81	1.25	0.77	0.63	0.93	1.24	0.59	1.11	1.15
TiO_2	2.11	2.26	2.19	2.21	2.26	2.21	2.31	2.35	2.27	2.61	2.11	2.26	3.15	1.97	2.14	3.22
MnO	0.18	0.19	0.17	0.18	0.23	0.19	0.18	0.21	0.17	0.21	0.19	0.19	0.23	0.19	0.19	0.22
P_2O_5	0.496	0.422	0.423	0.404	0.834	0.525	0.451	0.455	0.658	0.489	0.389	0.50	0.768	0.352	0.591	0.602
H_2O^-	0.42	0.22	0.58	0.78	0.22	0.41	0.19	0.18	0.95	0.17	0.42	0.41	0.17	0.25	0.27	0.15
H_2O^+	0.46	0.08	1.64	1.65	0.25	0.89	0.01	0.2	2.34	0.25	0.38	0.74	0.36	0.52	0.65	0.01
$\sum$	98.75	99.27	100.00	99.80	99.15	98.84	99.82	99.80	100.09	99.04	98.94	99.41	98.88	97.46	98.41	100.36
Mg#	55	54	53	52	40	57	51	50	50	47	52	51.00	38	55	54	37
Cr	360	390	300	270	240	360	280	330	190	180	220	283.64	90	280	440	70
Ni	126	156	124	118	38	153	118	113	82	67	84	107.18	25	116	129	16
Rb	18.9	13.1	12.7	12.8	23.6	18.8	14.1	13	22	12.4	9.6	15.55	20.9	10.2	19.3	18
Sr	698	596	782	773	678	667	592	647	825	575	538	670.09	571	465	749	588
Ba	260	216	200	188	425	455	199	232	319	194	158	258.73	310	162	293	234
Zn	86	94	89	89	107	99	92	98	89	117	102	96.55	143	99	89	114
Nb	37.2	29.8	30.6	29.9	46.6	39.2	31.2	30.1	46.1	25.8	20.7	33.38	38.5	19.4	36.5	37.5
Y	25.8	24.3	25.4	24.8	34.3	29.2	26.4	26.7	27.6	32.1	28.1	27.70	42.2	25.4	25.8	37.3
V	172	234	212	218	139	223	208	215	170	234	225	204.55	182	230	161	182
Cs	0.17	0.17	0.16	0.15	0.23	0.23	0.13	0.16	0.17	0.14	0.11	0.17	0.3	0.19	0.16	0.18
Sc	25	22	22	22	15	25	19	20	19	23	24	21.45	18	25	19	17
Co	41.8	52.5	46.3	46.9	36.3	50.7	47.8	50	39.5	50.4	51.6	46.71	44.1	51.3	44.6	41.9
Cu	76	72	68	76	40	66	65	68	54	49	51	62.27	45	68	51	34
Hf	4.7	4.3	4.5	4.4	6.3	5.1	4.4	4.3	5.3	4.9	4.1	4.75	6.8	3.7	5.3	6.4
Ta	2.3	1.8	1.8	1.8	2.9	2.3	1.9	1.8	2.7	1.6	1.3	2.02	2.4	1.2	2.4	2.4
Th	3.08	2.1	2.25	2.14	3.68	3.55	2.24	2.21	3.67	2.05	1.66	2.60	3.03	1.69	2.95	3.55
U	0.89	0.6	0.63	0.61	1.17	0.97	0.59	0.72	0.78	0.62	0.51	0.74	0.91	0.58	0.9	0.92
Zr	221	203	216	210	312	251	215	205	265	224	187	228.09	318	156	255	296
Mo	9	8	6	4	14	6	5	10	4	8	10	7.64	7	9	13	7
Sn	2	2	2	2	2	7	2	2	2	2	2	2.45	2	1	2	18
W	5	1	1	1	1	1	1	1	1	1	1	1.36	1	1	1	1
Mo	9	7	5	3	13	5	4	9	3	7	9	6.73	6	7	12	6
Be	1.5	1.2	1.3	1.4	2	1.4	1.2	1.3	1.7	1.3	1.1	1.40	1.9	1	1.6	1.8
Pb	2	6	3	2	3	6		4		4	3	3.00	4		2	15
S	0.07	0.03	0.01	0.01	0.24	0.07	0.01	0.06	0.02	0.12	0.21	0.08	0.04	0.21	0.18	0.02
As	9					6			5					11		
Cd										0.5						0.6
Sb							11		9	5						9
La	28.8	22.8	24.6	23.4	40	31.6	24.9	23.9	35.4	22.7	18.4	26.95	34.3	17	30.4	30.9
Ce	59.6	46.5	48.4	47.4	79.4	60.8	50	49.2	66.1	47.6	38.4	53.95	71.5	34.9	60.9	62
Pr	7.17	5.89	6.08	6	9.89	7.44	6.37	6.11	8.04	6.2	5.04	6.75	9.24	4.55	7.41	7.97
Nd	27.6	23.6	24.7	23.9	38.6	29.6	25.5	24.5	31.4	26.2	21.3	26.99	38	18.6	28.5	32
Sm	5.81	5.14	5.38	5.27	7.54	6.19	5.46	5.41	6.34	5.9	4.83	5.75	8.23	4.24	5.85	6.86
Eu	1.97	1.75	1.68	1.71	2.36	1.99	1.86	1.84	2.15	2.02	1.78	1.92	2.77	1.56	2.08	2.49
Gd	6.09	5.27	5.24	5.36	7.95	6.39	5.71	5.67	6.75	6.7	5.69	6.07	9.06	5.01	6.65	8.24
Tb	0.95	0.82	0.79	0.81	1.17	0.97	0.86	0.86	0.98	1.02	0.91	0.92	1.4	0.8	0.95	1.22
Dy	4.84	4.66	4.56	4.77	6.41	5.41	4.94	5.01	5.22	6.05	5.19	5.19	7.86	4.75	5.12	7.11
Ho	0.96	0.9	0.89	0.92	1.31	1.07	0.97	0.95	1.04	1.22	1.1	1.03	1.59	0.94	0.99	1.41
Er	2.9	2.54	2.52	2.61	3.82	3.04	2.78	2.72	3	3.47	3.1	2.96	4.54	2.81	2.84	4.28
Tm	0.43	0.34	0.34	0.35	0.54	0.42	0.36	0.36	0.39	0.47	0.4	0.40	0.64	0.38	0.38	0.55
Yb	2.45	2.23	2.1	2.15	3.31	2.66	2.26	2.22	2.44	3.1	2.85	2.52	3.98	2.42	2.38	3.84
Lu	0.39	0.33	0.33	0.33	0.51	0.4	0.34	0.34	0.37	0.48	0.44	0.39	0.63	0.39	0.36	0.57
Nb/Zr	0.17	0.15	0.14	0.14	0.15	0.16	0.15	0.15	0.17	0.12	0.11	0.15	0.12	0.12	0.14	0.13
La/Yb	11.76	10.22	11.71	10.88	12.08	11.88	11.02	10.77	14.51	7.32	6.46	10.78	8.62	7.02	12.77	8.05
Dy/Yb	1.98	2.09	2.17	2.22	1.94	2.03	2.19	2.26	2.14	1.95	1.82	2.07	1.97	1.96	2.15	1.85
Ce/Y	24.33	20.85	23.05	22.05	23.99	22.86	22.12	22.16	27.09	15.35	13.47	21.57	17.96	14.42	25.59	16.15

(*continued on next page*)

Table 2 (*continued*)

Q1	Q1	Q1	Q2	Q2	Q2	Q2	Q2	Q2	Q3	Q3	Q3	Q3	Q3	Q3	Q3	Q3
HL 32	HL 33	Q1 Average	HL 9	HL 14	HL 19	HL 27	HL 28	Q2 Average	HL 22	HL 23	HL 29	HL 30	HL 34	HL 35	HL 36	HL 41
25° 17.14′	25° 23.99′		24° 55.41′	24° 52.24′	24° 57.20′	25° 15.24′	25° 18.23′		25° 07.51′	25° 09.47′	25° 17.01′	25° 23.56′	25° 20.25′	25° 17.55′	25° 15.02′	25° 15.02′
37° 39.10′	37° 48.42′		37° 46.91′	37° 52.23′	37° 58.29′	37° 35.45′	37° 35.71′		37° 39.83′	37° 39.25′	37° 36.46′	37° 36.54′	37° 51.10′	37° 48.64′	37° 47.13′	37° 40.10′
45.18	45.58	45.38	46.12	47.08	46.46	45.85	45.57	46.22	45.52	45.04	47.08	45.75	45.41	45.04	44.37	45.18
16.25	16.49	16.11	16.09	16.74	16.32	15.7	15.98	16.17	15.92	15.94	16.51	15.91	16.59	16.15	16.39	15.85
15.11	12.98	13.83	11.69	12.72	13.39	10.96	12.66	12.28	15.37	12.61	12.21	12.94	15.88	15.9	13.78	12.7
8.51	9.78	8.97	10.26	8.23	9.4	11.79	10.03	9.94	7.77	10.6	9.22	9.77	7.79	8.04	8.97	10.13
5.78	7.07	6.12	6.61	6.1	7.34	7.22	7.93	7.04	4.87	8.13	6.2	8.09	5.01	4.9	4.38	7.97
3.8	3.74	3.81	3.63	4.21	3.52	2.72	3.18	3.45	4.05	2.96	3.66	3.36	4.2	4.06	4.11	3.19
0.84	0.76	0.95	1.01	1.07	0.74	0.64	0.62	0.82	1.12	0.54	1.01	0.79	1.14	1.15	1.06	0.68
2.72	2.25	2.58	2.03	2.29	2.45	1.76	1.96	2.10	3.25	2	2.15	1.94	3.26	3.24	2.69	1.97
0.22	0.19	0.21	0.2	0.2	0.2	0.18	0.19	0.19	0.23	0.19	0.19	0.2	0.23	0.24	0.22	0.2
0.497	0.42	0.54	0.604	0.588	0.404	0.307	0.405	0.46	0.734	0.307	0.582	0.453	0.755	0.773	0.714	0.432
0.15	0.2	0.20	0.16	0.16	0.11	0.43	0.21	0.21	0.15	0.15	0.42	0.24	0.17	0.21	0.47	0.23
0.09	0.11	0.29	0.1	0.01	0.01	1.27	0.24	0.33	0.25	0.06	0.82	0.34	0.09	0.38	0.69	0.27
99.15	99.57	98.97	98.50	99.39	100.33	98.83	98.98	99.20	99.23	98.53	100.05	99.78	100.53	100.08	97.84	98.80
43	52	47	53	49	52	56	55	53	39	56	50	55	38	38	39	55
190	210	213	300	260	250	410	340	312	130	270	250	380	120	140	160	330
36	98	70	113	96	103	141	138	118	33	127	77	149	29	31	23	127
11.9	11.5	15	17.4	18.3	11.7	10.2	8.6	13.24	17.8	8.2	13.5	12.7	16.4	18.4	16.2	10.4
585	580	590	596	584	509	557	582	566	546	519	609	550	565	554	652	563
205	171	229	307	212	158	401	171	250	279	140	253	224	278	319	264	189
117	94	109	93	96	108	88	92	95	141	91	96	95	138	138	122	104
29.1	23.8	30.8	37.7	35.3	24.6	20	20.4	27.6	36.4	17.6	42.4	27.8	39.1	37.9	33	22.2
31.9	26.1	31.5	29.8	30.8	30.4	27.1	25	28.6	41	24.8	29.6	26.3	39.5	40.6	36.9	24.9
219	197	195	194	188	256	247	203	217.6	205	236	184	191	196	186	135	196
0.12	0.12	0.18	0.21	0.16	0.11	0.14	0.1	0.144	0.2	0.1	0.11	0.15	0.17	0.25	0.22	0.1
19	22	20	24	18	26	33	24	25	18	26	21	21	18	18	15	22
49.3	48.1	46.6	43.1	43.7	53.1	46.4	49.3	47.12	45.9	54.1	39.8	49.5	45.2	45.3	38.4	49.1
33	61	49	58	65	60	86	66	67	46	63	50	55	41	43	34	61
5.1	4.2	5.3	4.9	5.4	4.5	3.6	3.7	4.42	6.3	3.4	5.2	4.1	6.3	6.3	6.3	3.6
1.8	1.5	2.0	2.3	2.3	1.6	1.2	1.3	1.74	2.2	1.1	2.6	1.7	2.4	2.4	2.1	1.3
2.2	1.95	2.6	3.22	2.73	1.88	1.74	1.68	2.25	2.74	1.38	3.77	2.33	2.87	3.01	2.66	1.79
0.65	0.61	0.76	0.94	0.8	0.54	0.41	0.5	0.64	0.82	0.43	0.87	0.69	0.83	0.93	0.94	0.6
226	189	240	243	262	200	153	167	205	309	153	240	186	297	295	286	170
13	7	9	5	8	6	7	9	7	9	7	9	12	9	10	12	12
2	2	5	2	2	3	1	1	1.8	2	2	2	2	2	2	2	1
1	1	1	1	1	1	1	1	1	1	1	1	1	1	1	1	5
12	6	8	4	8	5	5	8	6	8	6	7	10	7	7	10	12
1.4	1.2	1.5	1.5	1.6	1.2	1	1.1	1.3	1.7	1	1.5	1.2	1.7	1.8	1.8	1.1
2		4		2	2	4	7	3			4	2	5	7	5	
0.45	0.1	0.17	0.09	0.01	0.01	0.11	0.37	0.12	0.09	0.12	0.1 5	0.24	0.06	0.07	0.58 6	0.21
					5											
24.2	20.4	26.2	32.1	29	20.4	16.7	17.3	23.1	31.7	14.8	31.6	22.6	32.4	32.8	28.9	18.4
50	42	53.6	63	59	42.7	33	36	46.74	67	32.1	60.6	44.9	66.5	67.9	60.5	40
6.29	5.25	6.79	7.56	7.33	5.6	4.19	4.53	5.84	8.63	4.09	7.15	5.53	8.7	8.73	7.85	5.12
25.9	21.5	27.4	29.1	28.9	23.1	17.4	18.7	23.44	35.3	17.4	27.9	22.4	35.4	36.5	32.4	20.6
5.74	4.89	5.97	6.1	6.11	5.23	4.07	4.24	5.15	7.92	4.08	5.67	4.75	7.63	7.86	7.08	4.95
2.1	1.86	2.14	1.97	2.11	1.96	1.56	1.65	1.85	2.68	1.55	2.1	1.76	2.65	2.76	2.47	1.63
6.86	5.74	6.93	6.51	6.53	6.2	5.12	5.16	5.90	8.85	4.9	6.57	5.71	8.62	8.94	8.15	5.24
1.02	0.88	1.05	0.95	0.99	0.99	0.81	0.81	0.91	1.34	0.78	0.98	0.86	1.29	1.35	1.22	0.85
6.13	5.09	6.01	5.47	5.87	5.75	5.03	4.82	5.39	7.61	4.7	5.53	4.99	7.51	7.64	7.18	4.51
1.23	1.02	1.20	1.08	1.16	1.18	1.04	0.99	1.09	1.53	0.96	1.1	1.02	1.52	1.5	1.44	0.93
3.61	2.98	3.51	3.16	3.47	3.44	3.11	2.84	3.20	4.5	2.74	3.28	3.01	4.29	4.48	4.15	2.8
0.49	0.41	0.48	0.44	0.46	0.48	0.41	0.37	0.43	0.59	0.38	0.45	0.39	0.61	0.62	0.57	0.34
3.3	2.58	3.08	2.81	3.1	2.92	2.75	2.46	2.81	3.98	2.42	2.83	2.63	3.77	3.76	3.66	2.48
0.5	0.4	0.48	0.42	0.48	0.46	0.42	0.38	0.43	0.6	0.37	0.46	0.4	0.58	0.59	0.55	0.35
0.13	0.13	0.13	0.16	0.13	0.12	0.13	0.12	0.13	0.12	0.12	0.18	0.15	0.13	0.13	0.12	0.13
7.33	7.91	8.62	11.42	9.35	6.99	6.07	7.03	8.17	7.96	6.12	11.17	8.59	8.59	8.72	7.90	7.42
1.86	1.97	1.96	1.95	1.89	1.97	1.83	1.96	1.92	1.91	1.94	1.95	1.90	1.99	2.03	1.96	1.82
15.15	16.28	17.59	22.42	19.03	14.62	12.00	14.63	16.54	16.83	13.26	21.41	17.07	17.64	18.06	16.53	16.13

Formation	Q3	Q3	Q4	Q4	Q4	Q4	Q4	Q4	Q4	Q4	Q4	Q4	Q5	Q5	Q5	Q5
Sample	HL 43	Q3 Average	HL 12	HL 15	HL 16	HL 24	HL 26	HL 37	HL 38	HL 39	HL 42	Q4 Average	HL 1	HL 2	HL 40	Q5 Average
Latitude (N)	25° 08.35′		24° 55.32′	24° 52.80′	24° 58.97′	25° 09.99′	25° 14.13′	25° 12.34′	25° 10.44′	25° 13.91′	25° 14.15′		25° 04.45′	25° 02.91′	25° 07.65′	
Longitude (E)	37° 38.22′		37° 51.31′	37° 55.46′	37° 51.91′	37° 36.55′	37° 35.64′	37° 55.98′	37° 48.07′	37° 40.97′	37° 49.35′		37° 31.30′	37° 36.51′	37° 40.97′	
SiO_2	43.83	45.25	45.77	45.8	46.19	46.05	45.91	45.65	46.52	47.22	46.01	46.12	46.01	46.06	44.92	45.66
Al_2O_3	15.47	16.08	16.34	16.74	16.57	15.95	16.29	16.12	16.5	15.59	16.97	16.34	16.48	16.19	15.8	16.16
Fe_2O_3	9.8	13.47	13.95	13.79	14.33	15.62	14.34	12.46	14.47	15.61	11.62	14.02	13.89	14.1	13.02	13.67
CaO	12.84	9.46	9.33	9.19	8.7	7.26	9	10.36	7.93	7.3	10.71	8.86	8.68	8.6	10.7	9.33
MgO	6.18	6.19	6.67	6.15	6.83	4.48	3.69	8.66	4.42	4.32	8.21	6.29	6.53	6.96	7.98	7.16
Na_2O	3.03	3.62	3.56	3.62	3.71	4.26	3.69	2.94	4.2	4.09	2.88	3.66	3.7	3.64	3	3.45
K_2O	0.89	0.93	0.74	0.75	0.74	1.32	0.73	0.51	1.15	1.43	0.36	0.86	0.9	0.89	0.58	0.79
TiO_2	1.65	2.46	2.47	2.56	2.52	3.18	2.53	1.86	3.05	3.2	1.63	2.56	2.71	2.72	2.01	2.48
MnO	0.16	0.21	0.21	0.2	0.21	0.25	0.21	0.19	0.21	0.24	0.18	0.21	0.21	0.21	0.2	0.21
P_2O_5	0.433	0.58	0.434	0.468	0.432	0.865	0.409	0.275	0.782	0.792	0.22	0.52	0.488	0.487	0.333	0.44
H_2O^-	0.68	0.30	0.15	0.22	0.11	0.17	0.12	0.33	0.25	0.15	0.24	0.19	0.06	0.13	0.24	0.14
H_2O^+	1.92	0.54	0.12	0.04	0.01	0.35	0.01	0.14	0.3	0.01	0.29	0.14	0.03	0.01	0.18	0.07
∑	96.88	99.08	99.74	99.53	100.34	99.76	100.12	99.50	99.78	99.94	99.32	99.78	99.69	99.99	98.96	99.55
												0.00				0.00
Mg#	56	47	49	47	49	36	48	58	38	35	59	46.56	48	49	55	50.67
Cr	290	230	200	220	220	150	180	270	70	70	190	174.44	160	190	230	193.33
Ni	99	77	87	66	87	27	85	129	31	19	123	72.67	78	92	120	96.67
Rb	17.3	14.5	11.3	11.7	10.9	22	10.7	7.6	17.3	23.6	4.9	13.33	13.8	14.4	8	12.07
Sr	576	570	579	580	527	555	544	492	588	468	484	535.22	541	523	471	511.67
Ba	257	245	179	181	171	339	160	107	311	347	93	209.78	213	207	139	186.33
Zn	82	112	112	108	116	149	105	91	133	161	89	118.22	133	115	101	116.33
Nb	35.8	32.47	23.5	25.4	23.7	42.7	23.7	14.4	52.2	40.9	11.5	28.67	28.2	47.6	17.5	31.10
Y	22.2	31.76	30.7	31.2	30.7	45.1	29.6	21	41	48.1	20.6	33.11	28.8	40.9	23.8	31.17
V	163	188.00	245	234	249	152	233	213	175	169	213	209.22	206	216	223	215.00
Cs	0.27	0.17	0.14	0.13	0.13	0.29	0.1	0.11	0.18	0.28	0.04	0.16	0.14	0.12	0.07	0.11
Sc	22	20.11	23	22	23	17	24	27	19	20	27	22.44	22	23	27	24.00
Co	35.2	44.72	53.2	50.2	54.3	42.1	50.9	50.9	39.7	39.4	50.3	47.89	46.1	49.4	50.9	48.80
Cu	59	50.22	55	51	52	39	49	73	44	40	60	51.44	54	58	68	60.00
Hf	4.5	5.11	4.7	4.4	4.5	7.3	4.4	2.9	6.5	7.9	2.6	5.02	4.3	4.7	3.4	4.13
Ta	2	1.98	1.5	1.6	1.5	2.6	1.5	0.8	4.1	2.4	0.7	1.86	1.6	2.8	1.1	1.83
Th	3.84	2.71	1.87	1.87	1.68	3.39	1.76	1.27	3.21	4.69	0.9	2.29	2.25	5.64	1.38	3.09
U	0.89	0.78	0.64	0.6	0.46	1.07	0.5	0.36	2.75	1.18	0.26	0.87	0.65	14.6	0.45	5.23
Zr	214	238.89	211	213	210	347	198	137	302	375	124	235.22	206	213	150	189.67
Mo	7	9.67	7	10	8	11	5	7	6	6	5	7.22	6	6	6	6.00
Sn	2	1.89	4	2	2	3	2	1	2	36	2	6.00	2	2	1	1.67
W	4	1.78	1	1	1	1	1	4	5	4	4	2.44	5	5	5	5.00
Mo	6	8.11	7	9	7	10	4	7	5	5	5	6.56	6	5	5	5.33
Be	1.5	1.48	1.2	1.3	1.2	2.1	1.2	0.9	1.8	2.1	0.7	1.39	1.3	1.3	1	1.20
Pb	2	2.78	2	5		5	2	3		34	2	5.89	2	3		1.67
S	0.01	0.16	0.2	0.17	0.02	0.09	0.02	0.07	0.06	0.03	0.22	0.10	0.01	0.01	0. 05	0.02
As					6					6		1.33				0.00
Cd										1.4		0.16				0.00
Sb						5						0.56				0.00
La	25	26.47	20.9	21.2	20.7	38.4	20.2	12.9	31.9	36.5	10.3	23.67	23.8	23.1	15.2	20.70
Ce	49.7	54.36	44.3	45.2	43.2	79.7	42.1	30.3	72.8	81.5	24.2	51.48	51.6	51.5	37	46.70
Pr	5.75	6.84	5.8	5.91	5.6	10.3	5.49	3.94	9.3	10.65	3.25	6.69	6.57	6.75	4.45	5.92
Nd	22	27.77	24.2	24.5	23.9	42.6	22.8	16.5	37.7	43.9	13.7	27.76	26.4	27.3	18	23.90
Sm	4.56	6.06	5.48	5.57	5.34	9.15	5.14	4.06	8.61	9.66	3.42	6.27	6.11	6.87	4.27	5.75
Eu	1.5	2.12	1.93	2.02	1.94	3.06	1.99	1.31	2.65	2.98	1.29	2.13	1.93	1.93	1.51	1.79
Gd	4.76	6.86	5.96	6.29	6.08	10.2	6.3	4.15	8.85	10.25	3.88	6.88	6.11	7.18	4.62	5.97
Tb	0.78	1.05	0.94	0.97	0.95	1.52	0.98	0.72	1.41	1.63	0.69	1.09	0.97	1.35	0.78	1.03
Dy	4.08	5.97	5.67	5.71	5.78	8.85	5.65	3.88	7.9	9.13	3.74	6.26	5.24	7.85	4.31	5.80
Ho	0.81	1.20	1.17	1.16	1.16	1.72	1.16	0.82	1.49	1.81	0.82	1.26	1.09	1.65	0.94	1.23
Er	2.51	3.53	3.38	3.4	3.33	5.1	3.42	2.4	4.46	5.23	2.46	3.69	3.25	4.86	2.68	3.60
Tm	0.29	0.47	0.47	0.47	0.44	0.7	0.47	0.32	0.59	0.66	0.3	0.49	0.42	0.65	0.37	0.48
Yb	2.19	3.08	2.96	3.01	2.91	4.49	2.97	2.07	4.06	4.79	1.98	3.25	2.76	4.18	2.37	3.10
Lu	0.33	0.47	0.45	0.47	0.45	0.71	0.45	0.31	0.6	0.74	0.31	0.50	0.42	0.64	0.34	0.47
Nb/Zr	0.17	0.14	0.11	0.12	0.11	0.12	0.12	0.11	0.17	0.11	0.09	0.12	0.14	0.22	0.12	0.16
La/Yb	11.42	7.79	7.06	7.04	7.11	8.55	6.80	6.23	7.86	7.62	5.20	6.35	8.62	5.53	6.41	6.85
Dy/Yb	1.86	1.93	1.92	1.90	1.99	1.97	1.90	1.87	1.95	1.91	1.89	1.73	1.90	1.88	1.82	1.87
Ce/Y	22.69	17.74	14.97	15.02	14.85	17.75	14.18	14.64	17.93	17.01	12.22	15.40	18.70	12.32	15.61	15.54

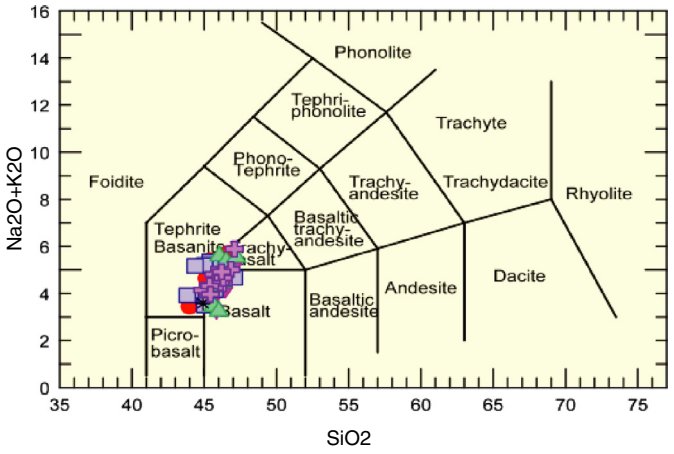

Fig. 7. Compositions of lavas at Harrat Lunayyir show a small range of variation, from basanites to alkali olivine basalts to trachy-basalts (after Le Bas et al., 1986), with no correlation to volcano-stratigraphic unit. Symbols are: T (purple cross), Q1 (red circle), Q2 (red diamond), Q3 (lavender square), Q4 (green triangle), and Q5 (black asterisk). (For interpretation of the references to color in this figure legend, the reader is referred to the web version of this article.)

variable compatibility in the mantle mineral garnet, Dy/Yb values significantly greater than 1 imply that at least some of the mantle melting that produced these magmas occurred within the garnet stability field (>60 km depth). The decreasing values with age indicate a possible diminishing influence of garnet, and thus shallowing of the source with time.

7. Discussion

The record of volcanic activity at Harrat Lunayyir provides valuable information about the processes responsible for magma generation above extending continental lithosphere. First, the short and recent timescale of eruptions, based on our new age determinations, shows that harrat activity is linked to present plate extension and/or mantle upwelling. The fact that magmas penetrate a continental shield (neo-Proterozoic metavolcanics and granite plutons) implies that the pre-existing condition was thick (>100 km), cold lithosphere that was subsequently modified to allow mantle melting and melt segregation at its base. Plate extension began about 30 Ma, centered on the Afar region, and developed into a triple junction of three

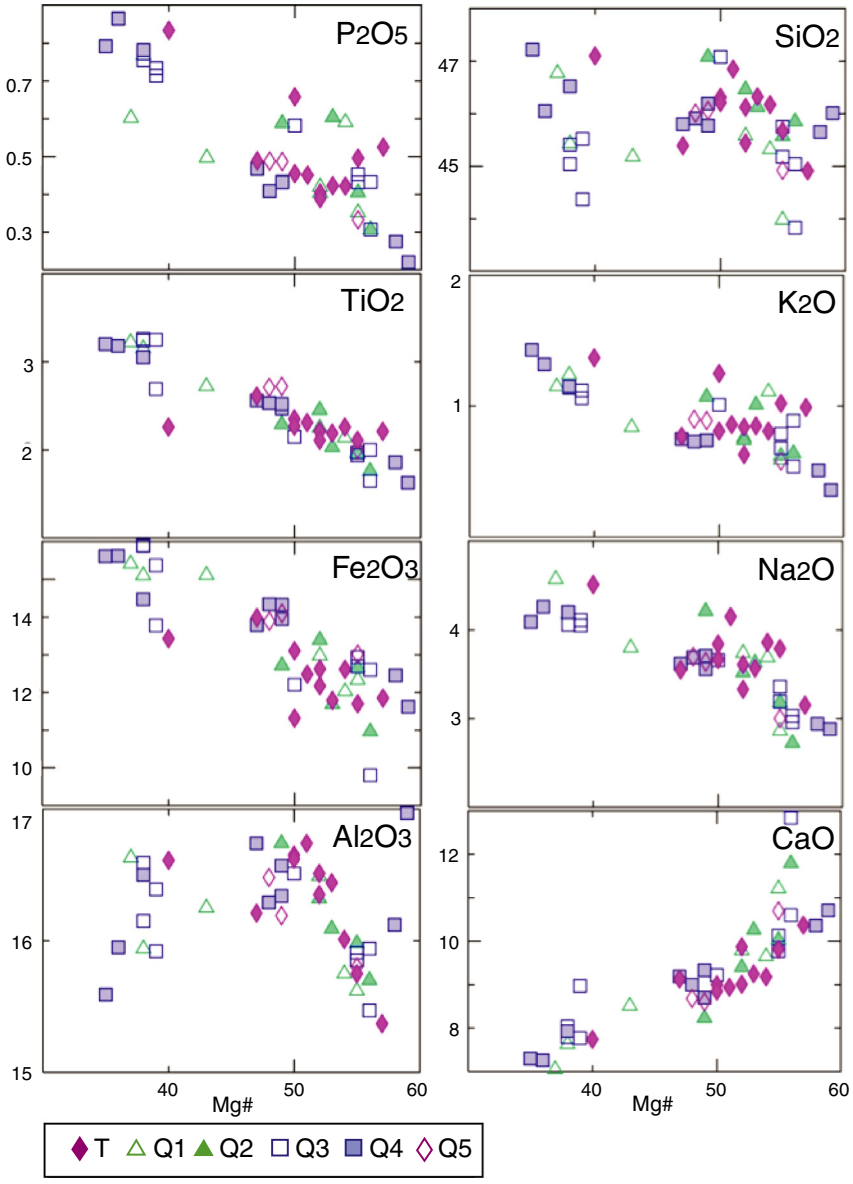

Fig. 8. Variation of major and minor element oxides with Mg# for Harrat Lunayyir lavas.

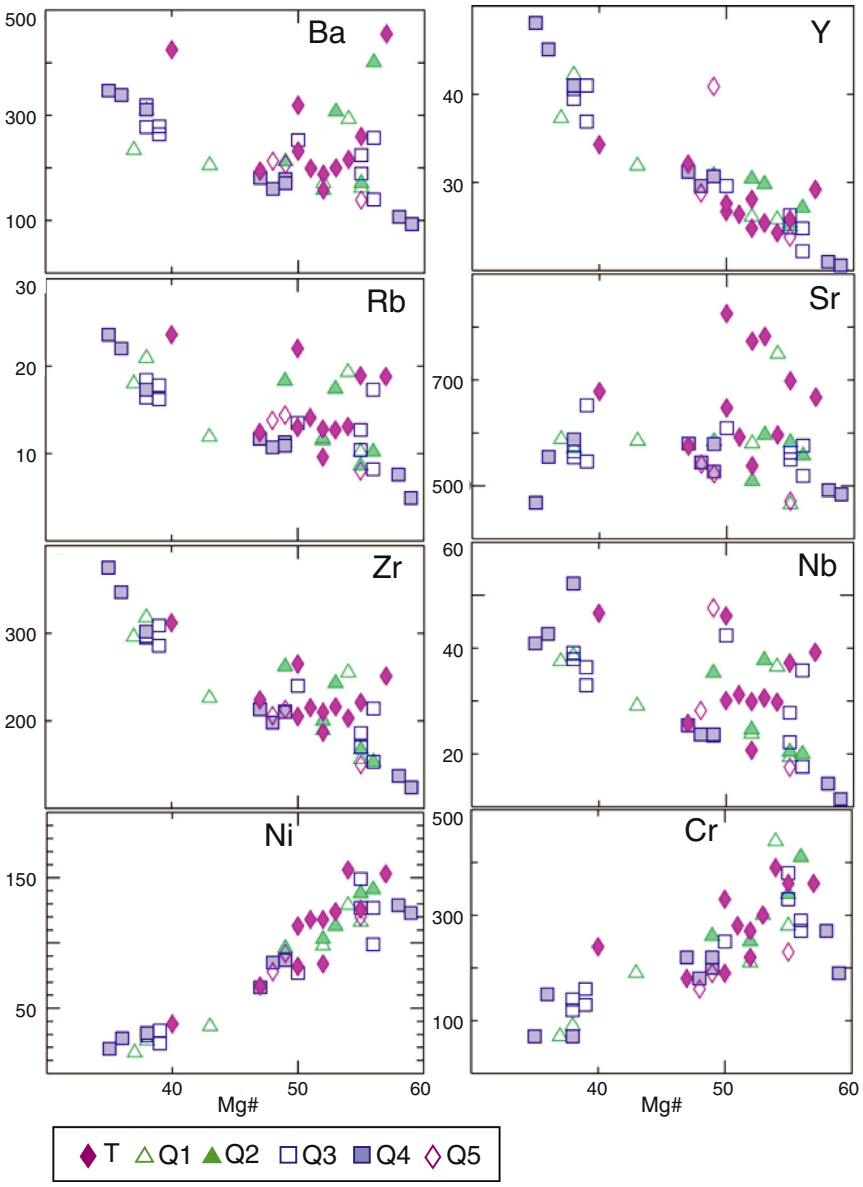

Fig. 9. Variation of selected trace elements with Mg# for Harrat Lunayyir lavas.

ridges — the Red Sea, the Gulf of Aden and the East African Rift. Full thinning and separation of the continental lithosphere has occurred in the Gulf of Aden and probably in the Red Sea, such that upwelled mantle is now melting at shallow depths beneath these two new spreading systems. The melting regime responsible for harrat volcanic activity, east of the Red Sea and within continental lithosphere, is less well understood, but geochemical data can constrain key parameters such as the depth of separation of magmas and the degree of melting of the mantle source.

The compositions of magmas formed by melting of upwelling mantle are strongly affected by source composition, extent of melting, and the depth of melting (McKenzie and Bickle, 1988; Ellam, 1992; Fram and Lesher, 1993). The concentrations of incompatible elements in residual mantle minerals are inversely correlated with the degree of partial melting, whereas the depth dependence of mantle mineralogy (plagioclase–spinel–garnet stability fields) produces predictable variations in major element concentrations and, especially, REE patterns. Ellam (1992) proposed the use of Ce/Yb and Sm/Yb, which are sensitive to the presence of garnet in the residual mantle (>60 km depth), as indicators of lithospheric thickness, both oceanic and continental. Relatively high ratios result from retention of heavy REEs (i.e., Yb) in garnet, and thus indicate greater depth of melt separation from the residual mantle, and vice versa. Ellam (1992) modeled fractional melting of an upwelling column of mantle to derive an integrated melt composition from onset of melting at ~125 km up to the base of the lithosphere, finding that Ce/Yb decreases smoothly with thinning lithosphere. Ce/Yb values for Harrat Lunayyir vary from 26 to 12, corresponding to melt separation depths of 80 to 60 km. Within the volcanic units there is a trend from higher to lower Ce/Yb (Fig. 6, unit T ave. = 21.6 to unit Q5 ave. = 15.5), suggesting a thinning of the lithospheric "lid" under Harrat Lunayyir with time.

Fram and Lesher (1993) built on this concept in interpreting the variation in basalt compositions erupted before, during and after continental thinning and plate separation in the North Atlantic in the construction of the East Greenland and NW British Tertiary flood basalt provinces, volcanic rifted margins and mid-ocean ridge basalts. Based on predicted magma compositions generated under varying upper mantle melt column conditions (e.g., Falloon et al., 1988;

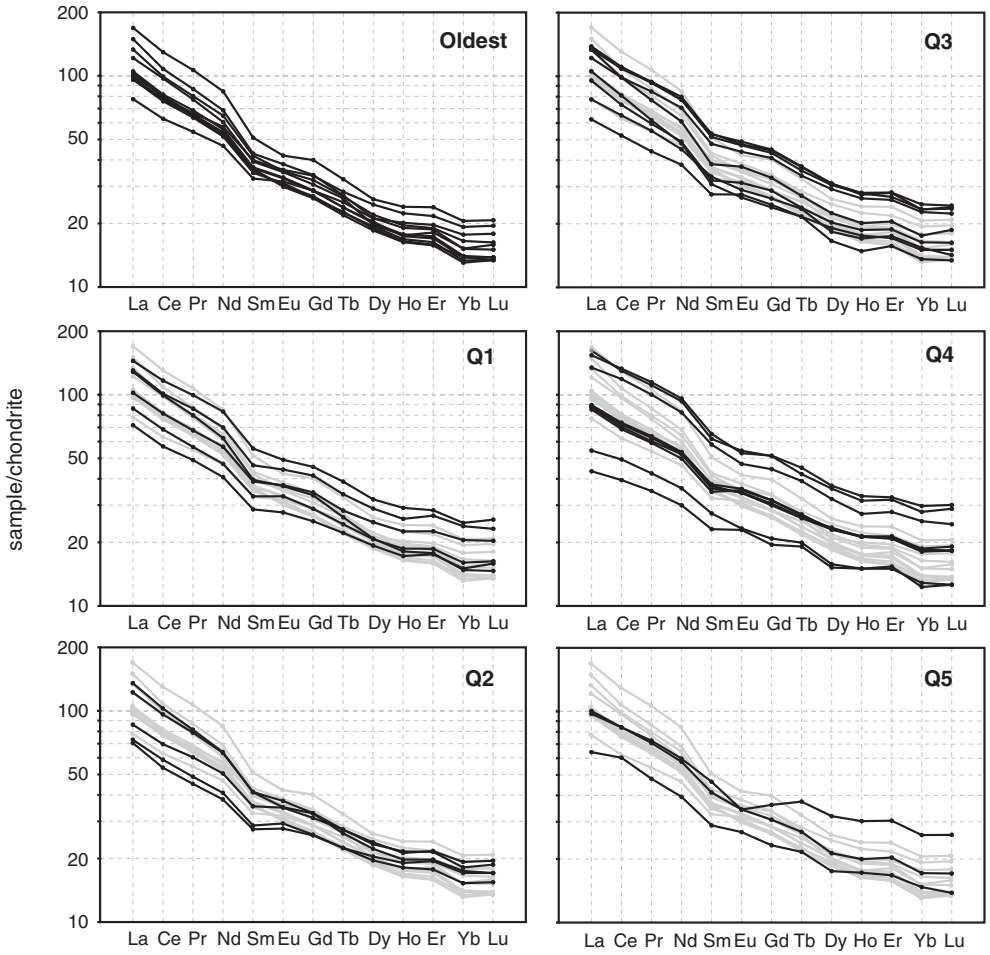

Fig. 10. Rare earth element concentrations, normalized to chondritic values (McDonough and Sun, 1995) in Harrat Lunayyir lavas show very coherent patterns, consistent with fractional crystallization of light rare earth enriched parental magmas in the shallow crust. In decreasing age, the units are Oldest (T), Q1, Q2, Q3, Q4, and Q5. The oldest set of patterns is also copied as light gray background in each of the 5 younger unit panels, to show that the slope of the patterns (e.g., La/Yb) decreases with time.

Kinzler and Grove, 1992) they concluded that earliest magmas were generated by lower degrees of partial melting at greater depth, while later magmas formed from higher degrees of mantle melting at lower pressures, consistent with decreasing lithospheric thickness. This example may provide an analog to the harrats of the western Arabian shield region, where variations in mantle melting occur beneath a thinning continental lithosphere. Fig. 11 (after Fram and Lesher, 1993) compares the compositions of magmas erupted during continental breakup in the North Atlantic with compositions from Harrat Lunayyir, neighboring Harrat Rahat (Camp et al., 1989), and Red Sea basalts (Essien et al., 1989). The compositional relationships show that depth of final melt segregation and degree of melting vary across this region, from ~25% melting at very shallow depths under the Red Sea spreading ridge, to 7–12% melting at 75–60 km depth under Harrat Lunayyir. Melting to produce lavas at Harrat Rahat, one of the large-volume MMN-lineament centers, appears to require larger degrees of melting (10–15%) at 20–40 km depth.

This modeling assumes a common mantle source for melting beneath the region, and predicts large variations in the depth of the lithosphere–asthenosphere boundary. In particular, continental lithosphere of the Arabian shield must thin from unmodified craton in the east to fully thinned (i.e., replaced by new oceanic lithosphere in the Red Sea) in the west. However, the region underlying the MMN lineament appears to have been thinned to a greater extent (now 20–40 km) than that under Harrat Lunayyir (60–75 km), in spite of the latter's closer proximity to the Red Sea. If Harrat Rahat lavas are representative of other centers in the MMN lineament, a N–S channel of thinned lithosphere appears to have formed under this region since 12 Ma.

Altherr et al. (1990) proposed a model of passive mantle upwelling in response to asymmetric extension (simple shear, Wernicke, 1981, 1985) to explain why volcanic activity occurred only on the east flank of Nubia–Arabia separation (i.e., initial Red Sea opening). This does not account for ongoing harrat volcanic activity, however, once plate separation focused on the Red Sea and mantle upwelling shifted westward to shallow depths to produce new ocean lithosphere. Nor does this model explain the change in orientation of volcanic centers from NW–SE, approximately parallel with the Red Sea margin, to N–S recently. The shallower and greater extents of mantle melting under the MMN-line compared to other harrat centers are not predicted by simple shear and plate thinning.

Contrasting models involve active upwelling. For example, Camp and Roobol (1992) and Krienitz et al. (2009) propose that radial flow of upper mantle material from the Afar mantle plume may have reached the base of the lithosphere beneath the Arabian shield, leading to excess heat, thinning, uplift and melting. Others (Moufti and Hashad, 2005; Chang and van der Lee, 2011) believe that a separate mantle plume, upwelling beneath the Arabian shield, may be implicated.

Geophysical methods provide images of the crust and upper mantle beneath the western Arabian shield, which must relate closely to the dynamic history of mantle flow, lithospheric uplift, and volcanic activity. Regional structure is known from seismic refraction studies

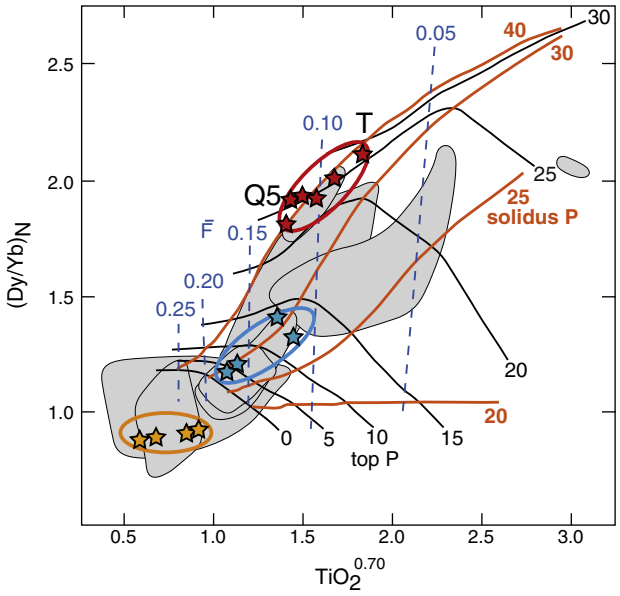

Fig. 11. $[Dy/Yb]_N$ is a measure of the slope of the heavy REE concentrations, which indicates the proportion of melting in the garnet stability field. $TiO_2^{0.70}$ is fractionation-corrected (to Mg# = 70) and indicates the degree of mantle melting. Background gray-shaded fields are from the volcanic margins of the North Atlantic (Greenland and Europe) and Iceland plus neighboring spreading ridges (from Fram and Lesher, 1993). The positive correlation results from the earliest (pre-rift) lavas generated by small degrees of melting at greater depths (upper right) to younger volcanic rifted margins and seafloor generated by larger degrees of melting at shallow depth (lower left). Superimposed are heavy curves showing depth of onset of melting (solidus, bold orange numbers in kbar), light curves showing the top of the melt zone (lithosphere thickness, black numbers in kbar), and dashed vertical lines are degree of melting (blue numbers are fractions). For comparison, Harrat Lunayyir unit compositions (red stars) plot in the red ellipse (25–20 kbar, or 75–60 km, 7–12% melting), Red Sea compositions (orange stars) plot in the orange ellipse (0 kbar, essentially no lithosphere, ~25% melting), and Harrat Rahat compositions (blue stars) plot in the blue ellipse (12–5 kbar, or 40–15 km, 10–15% melting). The T and Q5 labels over the red stars show the trend of compositions with decreasing age at Harrat Lunayyir. (For interpretation of the references to color in this figure legend, the reader is referred to the web version of this article.)

(Healy et al., 1982; Mooney et al., 1985; Gettings et al., 1986; Prodehl, 1986) and body and surface waves (Benoti et al., 2003; Julia et al., 2003). Additional information about upper mantle flow beneath the region comes from seismic anisotropy studies (Hansen et al., 2006, 2007). Recently, Chang and van der Lee (2011) report jointly inverted teleseismic S- and SKS-arrival times, regional S- and Rayleigh waveform fits, fundamental-mode Rayleigh-wave group velocities, and independent Moho constraints that provide complementary resolution for the three-dimensional (3-D) S-velocity structure beneath the region.

Specially, Chang and van der Lee (2011) find distinct low-velocity anomalies in the uppermost mantle, along with the shear-wave splitting results that suggest horizontal mantle flow radially away from Afar. This radial flow seems to be organized in channels, potentially following thin lithosphere. One such channel follows the Gulf of Aden, supporting the notion of eastward-directed mantle flow from Afar. Another channel extends northward beneath the southern Red Sea, but rather than following the NW-trending central and northern Red Sea, it continues northwards beneath western Saudi Arabia. A separate quasi-vertical low-velocity anomaly is found beneath Jordan and northern Arabia, possibly representing a separate mantle upwelling responsible for volcanic activity at Harrat Shamah in Jordan and Harrat Uwayrid in northern Arabia. This low-velocity anomaly extends significantly into the lower mantle, supporting geochemical evidence (Ilani et al., 2001) that the Neogene volcanism in Jordan has a deep mantle origin.

At present there is no strong geochemical evidence, such as excess mantle melting or distinct He-, Sr-, Nd- and Pb-isotopic compositions (Altherr et al., 1990), for involvement of Afar mantle plume material in the generation of harrat volcanic activity. Nor is there yet any clear temporal pattern of volcanic activity that might be related to age-progressive upper mantle flow beneath the Arabian shield. However, these data are lacking for many of the harrat centers, and future studies will focus on testing competing dynamic models.

8. Conclusions

The Harrat Lunayyir volcanic field is part of a larger Cenozoic province that reflects plate extension and thinning, and possibly regional mantle flow in the western Arabian shield region. Moreover, volcanic activity produced by these processes is ongoing. Although Harrat Lunayyir is one of the smaller fields, eruptions there have been among the most recent. The short volcanic record (~600 ka) indicates waning eruption rates, but the 2007–2009 seismic event presages new eruptions in the near future. The restricted range of basanitic and alkali basaltic lava compositions reflects generation from replenished, common parental magmas derived from ~10% partial melting of upper mantle peridotite at ≥60 km depth, followed by predominantly crustal level fractional crystallization. Trace element patterns (e.g., decreasing Ce/Yb with time) suggest a thinning of the lithosphere under Harrat Lunayyir. Comparison of lava compositions among volcanic fields across the region shows the effect of thinning lithosphere from the Arabian craton in the east to the new Red Sea oceanic lithosphere in the west. This simple pattern is interrupted, however, by a N–S axis of thinner lithosphere under the Makkah–Madinah–Nafud line of larger-volume harrat centers.

Acknowledgments

We express our gratitude to the Distinguished Scientist Fellowship Program (DSFP) at King Saud University for supporting this study and ongoing collaboration. We thank Dr. John Roobol for assistance in the field with sample collection, and to Mostafa Hemid and Musaed Al-Harbi for their contributions to seismic data collection and processing. We thank John Huard for sample preparation and analyses in $^{40}Ar/^{39}Ar$ age determinations. We thank reviewers Martin Menzies and Mariek Schmidt for their help in improving the manuscript.

References

Al-Amri, A.M., Fnais, M.S., Abdel-Rahman, K., Mogren, S., Al-Dabbagh, M., 2012. Geochronological dating and stratigraphic sequences of Harrat Lunayyir, NW Saudi. International Journal of Physical Science 7 (20), 2791–2805.

Altherr, R., Henjes-Kunst, F., Baumann, A., 1990. Asthenosphere versus lithosphere as possible sources for basaltic magmas erupted during formation of the Red Sea: constraints from Sr, Pb and Nd isotopes. Earth and Planetary Science Letters 96, 269–286.

Baker, J.A., Snee, L., Menzies, M., 1995. A brief Oligocene period of flood volcanism in Yemen — implications for the duration and rate of continental flood volcanism at the Afro-Arabian triple junction. Earth and Planetary Science Letters 138, 39–55.

Baker, J.A., Menzies, M.A., Thirlwall, M.F., MacPherson, C.G., 1997. Petrogenesis of Quaternary intraplate volcanism, Sana'a, Yemen: implications for plume–lithosphere interaction and polybaric melt hybridization. Journal of Petrology 38, 1359–1390.

Benoti, M.H., Nyblade, A.A., VanDecar, J.C., Gurrola, H., 2003. Upper mantle P wave velocity structure and transition zone thickness beneath the Arabian Shield. Geophysical Research Letters 30, 1–4.

Bertrand, H., Chazot, G., Blichert-Toft, J., Thoral, S., 2003. Implications of widespread high-μ volcanism on the Arabian Plate for Afar mantle plume and lithosphere composition. Chemical Geology 198, 47–61.

Bohannon, R.G., Naeser, C.W., Schmidt, D.L., Zimmermann, R.A., 1989. The timing of uplift, volcanism and rifting peripheral to the Red Sea: a case for passive rifting? Journal of Geophysical Research 94, 1683–1701.

Camp, V.E., Roobol, M.J., 1992. Upwelling asthenosphere beneath western Arabia and its regional implications. Journal of Geophysical Research 97, 15,255–15,271.

Camp, V.E., Hooper, P.R., Roobol, M.J., White, D.L., 1987. The Madinah eruption, Saudi Arabia: magma mixing and simultaneous extrusion of three basaltic chemical types. Bulletin of Volcanology 49, 489–508.

Camp, V.E., Roobol, V.E., Hooper, P.R., 1989. The Arabian continental alkali basalt province: part I. Evolution of Harrat Rahat, Kingdom of Saudi Arabia. Bulletin Geological Society of America 101, 71–95.

Camp, V.E., Roobol, M.J., Hooper, P.R., 1991. The Arabian continental alkali basalt province: part II. Evolution of Harrats Khaybar, Ithnayn, and Kura, Kingdom of Saudi Arabia. Geological Society of America Bulletin 103, 363–391.

Chang, S.-J., van der Lee, S., 2011. Mantle plumes and associated flow beneath Arabia and East Africa. Earth and Planetary Science Letters 302, 448–454.

Coleman, R.G., 1993. Geological evolution of the Red Sea. Oxford Monographs on Geology and Geophysics, no. 24. Oxford University Press, New York (186 pp.).

Courtillot, V., Achache, J., Landre, F., Bonhommet, N., Galibert, P.Y., Montigny, R., Feraud, G., 1984. Episodic spreading and rift propagation: new paleomagnetic and geochronologic data from the Afar nascent passive margin. Journal of Geophysical Research 88, 3315–3333.

Debayle, E., Leveque, J.J., Cara, M., 2001. Seismic evidence for a deeply rooted low-velocity anomaly in the upper mantle beneath the northeastern Afro/Arabian continent. Earth and Planetary Science Letters 193, 423–436.

Duncan, R.A., Keller, R.A., 2004. Radiometric ages for basement rocks from the Emperor Seamounts, ODP Leg 197. Geochemistry, Geophysics, Geosystems 5. http://dx.doi.org/10.1029/2004GC000704 (Art. No. Q08L03).

Ellam, R.M., 1992. Lithospheric thickness as a control on basalt geochemistry. Geology 20, 153–156.

Essien, J.-P., Juteau, T., Joron, J.-J., Dupre, B., Humler, E., Al'Mukhamedov, A., 1989. Petrology and geochemistry of basalts from the Red Sea axial rift at 18°N. Journal of Petrology 30, 791–839.

Falloon, T.J., Green, D.H., Hatton, C.J., Harris, K.L., 1988. Anhydrous partial melting of a fertile and depleted peridotite from 2 to 30 kb and application to basalt petrogenesis. Journal of Petrology 29, 1257–1282.

Fram, M.S., Lesher, C.E., 1993. Geochemical constraints on mantle melting during creation of the North Atlantic basin. Nature 363, 712–715.

Gettings, M.E., Blank, H.R., Mooney, W.D., Healey, J.H., 1986. Crustal structure of southwestern Saudi Arabia. Journal of Geophysical Research 91, 6491–6512.

Ghiorso, M.S., Hirschmann, M.M., Reiners, P.W., Kress, V.C., 2002. The pMELTS: a revision of MELTS for improved calculation of phase relations and major element partitioning related to partial melting of the mantle to 3 GPa. Geochemistry, Geophysics, Geosystems 3 (paper 2001GC000217).

Hansen, S.E., DeShon, H.R., Driskell, M.M., Al-Amri, A.M., 2013. Investigating P-wave velocity structure beneath Harrat Lunayyir, northwestern Saudi Arabia, using double-difference tomography and earthquakes from the 2009 seismic swarm. J. geophys. Res. (in press).

Hansen, S., Schwartz, S., Al-Amri, A., Rodgers, A., 2006. Combined plate motion and density driven flow in the asthenosphere beneath Saudi Arabia: evidence from shear-wave splitting and seismic anisotropy. Geology 34 (10), 869–872.

Hansen, S., Rodgers, A., Schwartz, S., Al-Amri, A., 2007. Imaging ruptured lithosphere beneath the Red Sea and Arabian Peninsula. Earth and Planetary Science Letters 259, 256–265.

Healy, J.H., Mooney, W.D., Blank, H.R., Gettings, M.E., Kohler, W.M., Lamson, R.J., Leone, L.E., 1982. Saudi Arabian Seismic Deep-Refraction Profile: Final Project Report. Ministry of Petroleum and Mineral Resources, Deputy Ministry for Mineral Resources, Kingdom of Saudi Arabia (Open File Report USGS-OF-02-37, 141 pp.).

Hill, R.I., Campbell, I.H., Davies, G.F., Griffiths, R.W., 1992. Mantle plumes and continental tectonics. Science 256, 186–193.

Ilani, S., Harlavin, Y., Trawneh, K., 2001. New K–Ar ages of basalts from the Harrat Ash Shaam volcanic field in Jordan: implications for the span and duration of the upper-mantle upwelling beneath the western Arabian plate. Geological Society of America Bulletin 89, 1025–1036.

Irvine, T.N., Baragar, W.R.A., 1971. A guide to the chemical classification of the common volcanic rocks. Canadian Journal of Earth Sciences 8, 523–548.

Julia, J., Ammon, C., Herrmann, R., 2003. Lithosphere structure of the Arabian Shield from the joint inversion of receiver functions and surface-wave group velocities. Tectonophysics 371, 1–21.

Kinzler, R.J., Grove, T.L., 1992. Primary magmas of mid-ocean ridge basalts 1. Experiments and methods. Journal of Geophysical Research 97, 6885–6906.

Koppers, A.A.P., 2002. ArArCALC — software for Ar-40/Ar-39 age calculations. Computers and Geosciences 28, 605–619.

Krienitz, M.-S., Haase, K.M., Mezger, K., van den Bogaard, P., Thiemann, V., Shaikh-Mashail, M.A., 2009. Tectonic events, continental intraplate volcanism, and mantle plume activity in northern Arabia: constraints from geochemistry and Ar–Ar dating of Syrian lavas. Geochemistry, Geophysics, Geosystems 10. http://dx.doi.org/10.1029/2008GC002254.

Le Bas, M.J., Lemaitre, R.W., Streckeisen, A., Zanettin, B., 1986. A chemical classification of volcanic rocks based on the total alkali silica diagram. Journal of Petrology 27, 745–750.

McDonough, W.F., Sun, S.-S., 1995. Composition of the earth. Chemical Geology 120, 223–253.

McKenzie, D., Bickle, M.J., 1988. The volume and composition of melt generated by extension of the lithosphere. Journal of Petrology 29, 625–679.

Min, K.W., Mundil, R., Renne, P.R., Ludwig, K.R., 2000. A test for systematic errors in Ar-40/Ar-39 geochronology through comparison with U/Pb analysis of a 1.1-Ga rhyolite. Geochimica et Cosmochimica Acta 64, 73–98.

Mooney, W.D., Gettings, M.E., Blank, H.R., Healy, J.W., 1985. Saudi Arabian seismic deep refraction profile: a travel-time interpretation of crust and upper mantle structure. Tectonophysics 111, 173–246.

Moufti, M.R.H., Hashad, M.H., 2005. Volcanic hazards assessment of Saudi Arabian Harrats: geochemical and isotopic studies of selected areas of active Makkah–Madinah–Nafud (MMN) volcanic rocks. Final Project Report (LGP-5-27). King Abdulaziz City for Science and Technology, Riyadh, Saudi Arabia.

Pallister, J., McCausland, W., Jónsson, S., Lu, Z., Zahran, H.M., El-Hadidy, S., Aburukbah, A., Stewart, I., Lundgern, P., White, R., Moufti, M., 2010. Broad accommodation of rift-related extension recorded by dyke intrusion in Saudi Arabia. Nature GeoscienceMacmillan Publishers Limited (8 pp.).

Prodehl, C., 1986. Interpretation of a seismic-refraction survey across the Arabian Shield in western Saudi Arabia. Tectonophysics 111, 247–282.

Renne, P.R., Swisher, C.C., Deino, A.L., Karner, D.B., Owens, T.L., DePaolo, D.J., 1998. Intercalibration of standards, absolute ages and uncertainties in Ar-40/Ar-39 dating. Chemical Geology 145, 117–152.

Schilling, J.-G., 1973. Afar mantle plume: rare earth evidence. Nature 242, 2–6.

Shaw, J.E., Baker, J.A., Menzies, M.A., Thirlwall, M.F., Ibrahim, K.M., 2003. Petrogenesis of the largest intraplate volcanic field on the Arabian Plate (Jordan): a mixed lithosphere–asthenosphere source activated by lithospheric extension. Journal of Petrology 44, 1657–1679.

Steiger, R.H., Jäger, E., 1977. Subcommission on geochronology: convention on the use of decay constants in geo- and cosmochronology. Earth and Planetary Science Letters 114, 193–209.

Wernicke, B., 1981. Low-angle normal faults in the Basin and Range Province: Nappe tectonics in an extending orogen. Nature 291, 645–648.

Wernicke, B., 1985. Uniform-sense normal simple-shear of the continental lithosphere. Canadian Journal of Earth Sciences 22, 108–125.

Wijbrans, J.R., Pringle, M.S., Koppers, A.A.P., Scheevers, R., 1995. Argon geochronology of small samples using the Vulkaan argon laserprobe. Proceedings of the Koninklijke Nederlandse Akademie van Wetenschappen 98, 185–218.

York, D., 1969. Least squares fitting of a straight line with correlated errors. Earth and Planetary Science Letters 5, 320–324.